

Experimental characterization of a pump-turbine in pump mode at hump instability region

Yang J.

National Research Center of Pumps - Jiangsu University
Xuefu Road 301 - Zhenjiang 212013 – Jiangsu - China
jyang.tcpr@gmail.com

Pavesi G.¹

Department of Industrial Engineering, University of PADOVA, Italy
Via Venezia 1, 35131 Padova , Italy
giorgio.pavesi@unipd.it

Yuan S.

National Research Center of Pumps - Jiangsu University
Xuefu Road 301 - Zhenjiang 212013 – Jiangsu - China
shouqiv@uj.edu.cn

Cavazzini G.

Department of Industrial Engineering, University of PADOVA, Italy
Via Venezia 1, 35131 Padova , Italy
giovanna.cavazzini@unipd.it

Ardizzon G.

Department of Industrial Engineering, University of PADOVA, Italy
Via Venezia 1, 35131 Padova , Italy
guido.ardizzon@unipd.it

ABSTRACT

The unsteady phenomena of a low specific speed pump-turbine operating in pump mode was characterized by dynamic pressure measurements and high-speed flow visualization of injected air bubbles. Analyses were carried out on the pressure signals both in frequency and time-frequency domains and by bispectral protocol. The results obtained by high-speed camera were used to reveal the flow pattern in the diffuser and return vanes channels. The unsteady structure identified in the return vane channel appeared both at full and part load condition. Furthermore, a rotating stall structure was found and characterized in the

¹ Corresponding author: Prof .Giorgio Pavesi email: giorgio.pavesi@unipd.it,

diffuser when the pump operated at part load. The characteristics of these two unsteady structures are described in the paper.

Keywords: *pump-turbine, hump-instability region, pressure measurement, high-speed flow visualization, rotating stall*

INTRODUCTION

Pumped storage power plants can play an important role in stabilizing the electric power system fed by renewable energy sources such as wind and sun which have varying and, to some extent, unpredictable production.

The reversible pump turbine solution is widely regarded as one of the most cost effective solutions. Depending on reservoir size, it can deliver long term energy storage, and is able to boost production (turbine) or consumption (pump) in peak power situations. Although the pumped storage may solve some problems in the grid, pump-turbine operation and control can lead to other problems due to the rapid switching from pump to turbine mode and vice versa with extended operation at off-design condition.

Two main features of unstable behavior of pump turbines are identifiable:

- one occurring in generating mode at low load off-design operation close to runaway conditions (S-shape of the turbine characteristic)
- the other one occurring in pumping mode at part load (saddle-type pump instability of head curve – “hump” zone)

In pumping mode, the unstable behaviour is associated with a positive slope of the head-flow curve ($dH/dQ > 0$) and is undoubtedly one of the most challenging problems to face in order to significantly increase the stable operating range of pump-turbines in pumping mode, even in case of variable speed pump-turbine [1].

This unstable pump operating zone is characterized by a head drop associated with an increase of the hydraulic losses in the runner, in the stator parts or in both. At off design conditions, the diffuser and the draft tube do not work properly and give awkward boundary conditions to the runner, together with a strong fluid-dynamical interaction between runner and stator parts [2- 5]. The flow features such as separation and

recirculation occur severely in an unsteady manner. The guide vanes may experience strong vibrations and high cycle fatigue stress may result in the propagation of cracks and the failure of shear pin or guide vanes stem [6].

Among the phenomena developing inside the machine, the onset of a fluid-dynamical instability as a consequence of the rotor-stator interaction still represents a crucial point in the research field and authors are still debating on the reasons of its onset and development. Several experimental and numerical analyses have been carried out to identify a possible connection of unsteady flows and pressure fluctuations developing inside centrifugal pumps with runner/diffuser geometries and operating conditions.

González et al. [6] and Cavazzini et al. [7] study the dynamic and unsteady flow effects inside a centrifugal pump due to the runner-volute interaction. The results of both experimental and numerical analyses highlighted the existence of a spatial fluctuation pattern concentrated close to the runner exit, whose fluctuations levels increases at off-design conditions.

In 2002, Sano et al. [8] highlighted the significant influence of the gap between runner and diffuser on the development of flow instabilities in the vaned diffuser, such as the rotating stall, alternate blade stall and asymmetric stall. In particular the study demonstrated the development of a runner/diffuser coupled rotating stall in case of a small gap and the switching between reverse flow and jet flows in the diffuser channel during the rotating stall development. Alternate stalled and unstalled runner passages at part loads were observed by Pedersen et al. [9] , whose study presents one of the first experimental analysis capturing instantaneous flow fields inside the runner.

To better understand the effects of the diffuser blockage on the runner fluid-dynamics, Hong and Kang [10] carried out an experimental analysis to measure the flow field at the runner exit with and without a fence with sinusoidal width variation installed at the vaneless diffuser exit. The mean flow parameters, such as static pressure, total pressure and flow angles, resulted to be strongly dependent on the circumferential position. The circumferential distortion of the pressure distribution at the runner outlet due to the rotor-stator interaction was confirmed by Majidi [11]. Its study highlighted the existence

of pressure fluctuations, stronger at the runner outlet but spread to the runner inlet, affecting the mass flow rate through the runner blade passages and the runner blade loading. In particular, the flow unsteadiness was demonstrated to significantly amplify the blade loading fluctuations at off-design conditions, giving rise to important dynamic effects.

Due to the importance of the onset of dangerous dynamic effects, a significant interest in the spectral characterization of the unsteady pressure fluctuations due to the rotor-stator interaction started to grow. Guo and Maruta [13] investigated the onset of resonance phenomena as a consequence of the circumferential unevenness of the pressure fluctuations, whereas Rodriguez et al. [13] presented an interesting theoretical method to predict and explain the possible harmonics that could appear in a pump-turbine as a consequence of the interaction between moving and stationary blades.

The frequency content of the pressure fluctuations was analysed both in frequency and in the time-frequency domains by Pavesi et al. [14], whose study presented a spectral analysis of the unsteady phenomena developing in a pump-turbine. Their analysis highlighted the existence of a rotating structure of pressure pulsations at the runner exit appearing and disappearing in time, having greater intensity at part loads. This strong RSI, experienced by several authors at off-design conditions, resulted to be further emphasized in multi-stage pump-turbines in which a 'full-load-instability' (FLI) develops in the range from 60 to 90% of the design flow rate [15].

Even though the experimental analyses allowed to identify and characterize the development of unsteady pressure pulsations in the hump zone of the pump-turbine operating range, a significant boost to the understanding of this instability was provided by Computational Fluid Dynamics, whose ability and capability of modeling the flow through the entire machine in a single CFD simulation was significantly increased in the last years. Cavazzini et al. [16] carried out a numerical analysis at an unstable operating point of a multi-stage pump-turbine, identifying the pulsating onset of reverse flow cells in the runner, moving along the blade length and from one channel to another. This unsteady behavior in the runner resulted to be associated with a perturbation of the

diffuser flow field, characterized by unsteady flow rate migrations between passages and by unsteady flow jets. Numerical analysis were also carried out by Gentner et al. [17] highlighting the dependence of the flow behaviour in the head drop from the specific speed of the pump-turbine, whereas Pavesi et al [25] analyzed the influence of two rotational speed on the inception and evolution of the pressure instabilities.

More recently, Li Deyou et al [26] focused the numerical analyses into the hump region trying to correlate the hump characteristics to the vortex motion in the tandem cascade. Even though these studies have allowed to obtain interesting information on the unstable behavior of pump-turbines, to solve instability problems and to significantly enlarge the working range of pump-turbine, an in-depth understanding of the unsteady flow mechanism at hump points is crucial for the production stabilization.

The aim of this investigation is to analyse the characteristics of the instabilities of a two stages reversible-pump turbine operating in pump-mode and to study the development of the unsteady phenomena. The experimental research included the dynamic pressure measurements and high-speed flow visualizations from design to part flow rate. The analysis of pressure fluctuations were conducted both in frequency and time frequency domain and the flow visualization was focused in the diffuser and in return channel.

EXPERIMENTAL SET-UP

The experimental analyses were carried out in the Open Turbomachinery Facility (OTF) of the Department of Industrial Engineering of the University of Padova. The OTF is a water test rig designed for testing the influence of several parameters on the overall performance of both pumps and turbines.

The analyzed pump-turbine was the low-pressure stage of a two stages pump-turbine operating in pump mode. The scaled down model consists of a shrouded radial impeller, shown in figure 1, with seven 3 D backward swept blades with a discharge angle of 26.5° , referred to the tangent and a design specific speed $n_s = 37.6 \text{ m}^{0.75} \text{ s}^{-1}$. (dimensionless design specific speed $\omega_s = 0.71$).

Refeeding channels were used to guide the flow that leaves the impeller to the inlet of the subsequent channel. The channels were made up of 22 adjustable guide-diffuser

vanes and 11 continuous vanes. The guide-diffuser allows continuous and independent adjustment of the vane angle and of relative azimuthal position with the return channel vanes. The radial gap between the impeller tip and the inlet edge of the stator vanes, for the configuration under test with the vane angle rotated of 18° from the fully closed position, was about 10.5 mm, which is 5.25% of the impeller radius. The relative azimuthally position of the diffusers vanes was fixed rotating the system of 8 degrees from the face to face configuration (reference position with $\lambda=0^\circ$, fig. 2) corresponding to the configuration with the highest efficiency in turbine mode.

Geometry characteristics of the tested pump-turbine were listed in table 1.

The unsteady pressure was measured at the mid-height of a diffuser guide vane (the gray vane in Fig. 1) with 12 piezoresistive transducers Kulite XCL-072 (sensitivity of about 29.3 mV/bar), which were faced mounted as schematized in Fig. 2. The combined non-linearity, hysteresis, and repeatability of the sensors were better than $\pm 0.1\%$. The data of the sensors were simultaneously acquired at a sampling rate of 1024 Hz for 256 sampling times of 8 s each, and recorded by a workstation-controlled transient data recorder, with a dynamic range of 24-bit.

To evidence and describe the flow field into the passage between the diffuser and return channel vanes, high-speed flow visualizations were performed. For this purpose, a Photron FASTCAM PCI digital camera was used and the video camera recorded images at full resolution (512×512 pixels) with a frame rate 5000fps and a shutter 1/5000. Two tungsten halogen bulbs with 1000W were used to provide the light of the scene. A needle valve was employed to control the amount of injected air throughout holes of 0.5 mm diameter located in the mid span of the diffuser and return channel vanes located in the same positions of the pressure transducers, as shown in Fig. 2. The injection pressure was maintained at a value slightly above the mean pressure at the injection location.

The motion of air bubbles was theoretically analyzed for a radial pump by Minemura and Murakami [24]. They solved the equation of motion for air bubbles in the flow field including the effects of the drag force and slip, density differences between the phases

and inertia force. By comparing their results to the experimental data, they demonstrated that the bubble motion within the impeller is controlled by the corresponding drag force and the pressure gradient around the bubble. The tendency that bubbles deviate from the streamlines of liquid water raises with increasing bubble diameter. Until the dimension of the single bubble was small in the following analyses it was assumed that the air bubbles fairly follow the streamlines with almost no effect on the flow itself.

A stroboscopic light was also used to estimate the frequency oscillation of the back flow zones.

PRESSURE SIGNAL PROCESSING

The pressure signals were analyzed in both the frequency domain and the time–frequency domains to identify and characterize the unsteady phenomena in the saddle region. The power spectra were computed by partitioning each time signal into 2^8 segments of 2^{10} samples with overlapping percent 50%, filtered with a Hanning window for avoiding aliasing and leakage errors. The frequency resolution was 0.125Hz. The auto-spectra and the cross-spectra were computed by the following equation [18]:

$$G_{xy}(f) = \frac{1}{NW_H} \sum_{k=1}^N [X_k^*(f)X_k(f)] \quad (1)$$

where N is the number of segments, W_H is weighting constant corresponding to the Hanning windows, $X_k(f)$ is the fast Fourier transform of the k^{th} data segment of the signal x , and $X_k^*(f)$ is the complex conjugate of $X_k(f)$.

Time-frequency analyses were carried out by the wavelet transforms to provide information on the variation of pressure spectral frequencies components versus time. The continuous wavelet transform $W(s, n)$ of the discrete sampled pressure signal x_n was computed via the FFT-based fast convolution:

$$W(s, n) = \sum_{k=0}^{N-1} X_k \left(\sqrt{\frac{2\pi s}{\delta t}} \psi_0^*(s\omega_k) e^{i\omega_k n \delta t} \right) \quad (2)$$

where s is the wavelet scale, n is the localized time index, k is frequency index, X_k is the discrete Fourier transform (DFT) of x_n , N is the data series length, δt is the sample time interval. $\sqrt{2\pi s/\delta t}$ is a normalization factor which could obtain unit energy at each scale. $\psi_0^*(s\omega_k)$ is the complex conjugate of the Fourier transform of the scaled version of the “mother wavelet” $\psi(t)$ and ω_k is the angular frequency. The choice of the mother wavelet depends on several factors [19] and in this paper complex Morlet wavelets were used with $2\pi f_0 = 6$, since it could provide a good balance between time and frequency localization and it returned information about both amplitude and phase. To determine the relation between two pressure signals in the time–frequency domains, the cross-wavelet spectrum was determined as [20]

$$W^{xy}(s, n) = W^x(s, n)W^{y*}(s, n) \quad (3)$$

Furthermore, in order to determine the non-linear and linear components in the frequency domain, bispectrum analysis was carried on in this paper.

Bispectral analysis is an advanced signal processing technique that quantifies quadratic nonlinearities and deviations from normality. The bispectrum $B(f_1, f_2)$ is a function of two frequency variable f_1 and f_2 and it was computed as [21]

$$B(f_1, f_2) = \left| \sum_{k=1}^N X_k(f_1)X_k(f_2)X_k^*(f_1 + f_2) \right| \quad (4)$$

RESULTS

Analysis of the pressure signals

The characteristics, evaluated in accordance with ISO standards, show slightly hump-type instabilities behaviour between $Q/Q_{Des} \approx 0.45$ to 0.70 (Figure 3). Below $Q/Q_{Des} \approx 0.40$ the characteristic raised due to the effect of fully developed inlet recirculation [14]. The mean pressure variation at the impeller outlet is shown versus the flow rate in figure 4.

The mean pressure fluctuation shows a slight but steady monotone increase with decreasing the flow rate not far from the design flow rate and a sharp increase when

the flow rate diminishes below to the critical value $Q/Q_{Des} \approx 0.7$ that is the same flow rate value where the head characteristic was observed unstable. Moreover, the pressure fluctuation intensity shows a discontinuity when the flow field shows a change from random instabilities (fig. 12) up the appearance of stall cells (fig. 14) as will be discussed in the following chapter.

In the same figure 4 the static pressure increase between impeller inlet and outlet was diagrammed versus the flow rate with the measured band of oscillation at impeller outlet. The data confirm the non monotonic increase of the pressure oscillation in the hump zone.

The analysis of the pressure signals of the experiment campaign, from 0.29 to 1.19 Q/Q_{Des} , was focused in this segment. Fig.5 shows the power spectrum of pressures measured by the transducer D5, D6, D11 and D12 in the diffuser vane (fig. 2). The spectra were dominated by the blade passage frequency (BPF, $St=1$) especially in the region closer to the impeller blade trailing edge, the impeller rotating frequency ($St_R \approx 0.143$), and two other frequency peaks. The main one at $St_F \approx 0.6625$ was observed in the flow interval $Q/Q_{Des} \approx 0.37$ to 1.19, the second one at $St_S \approx 0.335$ was observed in the flow interval $Q/Q_{Des} \approx 0.45$ to 0.75. Moreover, this variation is in agreement with the power spectrum amplitude variation of pressure at $St_R \approx 0.143$ and $St_F \approx 0.6625$ (Fig. 4). During the hump-type instabilities region, the value of mean pressure has a sharp decrease around 0.6 Q/Q_{Des} .

As demonstrated by Akin and Rockwell [22], an unsteady forced perturbation of the fluid flow in pump, generates non-linear interaction components in the power spectra.

The high order analysis highlighted (Fig. 6) that two different unsteady flow structures ($St_F \approx 0.6625$, $St_S \approx 0.335$) exist and interact with each other and with the blade passing frequency. Table 2 summarizes the identified independent component frequencies that were identified by the transducers D3, D5 and D6 at some flowrates. The $St_F \approx 0.6625$ represents a pressure fluctuation pointed out both at full and part load. The $St_S \approx 0.335$ was, as a fundamental frequency, present with flowrate below the critical value of $Q/Q_{Des} \approx 0.7$ and greater than $Q/Q_{Des} = 0.6$. The amplitude in $St_S \approx 0.335$ in all the other

flowrate was not a fundamental frequency but a nonlinear interaction between the components BPF and St_F ($St_{BPF}-St_F$). Decreasing the flowrate, the unsteady structure $St_S \approx 0.335$ disappeared around $0.60 Q/Q_{Des}$ (Fig. 7) and simultaneously the mean pressure variation decreases (Fig. 4).

The existence of this fluid-dynamical unsteadiness was confirmed by the time-frequency analysis carried out at all the flow rates. In the instabilities zone, the power of the pressure pulsation of St_F and St_S gradually increases with the decrease of flowrate up to $0.60 Q/Q_{Des}$. Fig. 7 shows the wavelets (transducer D6) at 0.62 , 0.60 and $0.59 Q/Q_{Des}$. The low frequency component St_S presents a non constant pulsating value at 0.62 and $0.60 Q/Q_{Des}$ while disappears at Q/Q_{Des} lower than 0.59

Fig. 8 shows the cross wavelet magnitude $|W_n|$ of the pressure at two flow rates in the instability zone. The subtonal components was periodically present at all measurement positions and coherent along the diffuser blade. When the flowrate reduces below $0.60 Q/Q_{Des}$ the effect of St_S progressively disappears (Fig. 7 (c)). At the same time, the cross-correlation at St_F gradually weakened.

Analysis of high-speed flow visualizations

Two different unsteady patterns were detected by the pressure analyses. To understand the development of these unsteady flow structures, analyses by high-speed flow visualizations were carried out with the field of vision zoomed in flow passage between the vanes of diffuser and return channel.

In the analysis of the frames was assumed that the air bubbles fairly follow the streamlines with almost no effect on the flow itself. The flow visualizations highlighted that the recirculation regions were present in the U-turn return channel at design and lower flow rate.

At full load condition, inside the diffuser vane channel, the trajectory of air bubbles from D4 hole was straight with a quite negligible longitudinally unsteadiness (Fig. 9a). In the return vane channel, the bubbles that were blown out of the hole R16 were rapidly scattered forming puffs of bubbles. The bubbles flow pattern was close to the diffuser suction side (Fig. 9b) and the frequency of the bubbles clouds was consistent with $St_F \approx$

0.6625. A reverse flow volume was present in the corner between the vane suction side and the U-Turn hub (central region in Fig. 9b). The bubbles, blown out the R16 hole, were partially absorbed by the reverse flow and moved inside it with an ellipsoidal path. By the use of a stroboscopic light this recirculation, showed a pulsating oscillation equal to the impeller rotating frequency ($St_R=0.143$).

Reducing the flow rate, at the beginning, the bubbles moved along the diffuser blade surface with random slowing down and restarting (Figs 10 b and c) as the solid line shown in Fig. 11. With a further reduction of the flow rate, the intensity of the pulsations increased, a flow separation began to appear around the trailing edge (Fig. 12) and gradually extended along the diffuser vane as sketched by the broken line in Fig. 11 and the bubbles paths into the diffuser became slightly unstable in the crosswise direction. Moreover, the back flow volume in the return channel moved along the suction side, extending towards both the runner and the outlet directions. The unsteady pattern in return channel strengthened emphasizing its characteristic frequency $St_F \approx 0.6625$ with the flow rate decreasing

At lower flow rate the flow field into the diffuser manifested a three-dimensional flow structure. At about $0.63 Q/Q_{Des}$, a crosswise unstable disturbance appeared, shown by the frames sequence in Fig. 12. The air bubbles were periodically spread out axially on the diffuser blade. This disturbance was related to the boundary layer separation and stall in the diffuser and was noticed with a frequency very close to $St_S \approx 0.335$.

Furthermore, an intermittent spiral trajectory started to appear at the inlet of return channels shown by the frames sequence in Fig. 13 and schematized in Fig 13a. In the same sequence three groups of bubbles are marked by A, B and C to help to identify the complex 3D trajectory. This macro vorticity is consistent with the progressive periodic partial choke of the diffuser vane. The increase of the intensity of the disturbances both into the diffuser and in the return channels is highlighted by the overall pressure fluctuation measured at the exit of the impeller and shown in fig. 4.

With a further flow rate reduction, the flow became more unstable. At $0.59 Q/Q_{Des}$, as shown in Fig. 14, the air injected through the hole D3 of the diffuser was found

periodically to move back toward the impeller. Each back flow sequence is staggered by a period during which the bubbles path is straight and undisturbed suggesting a rotating stall situation. The flow field evolved from a stochastic instability sequences able to generate an higher intensity of the overall pressure pulsation to a quasi periodic instability with a more limited oscillation of the head (fig. 2) and lower noise emission (fig. 4). The numerical analysis (Pavesi G. et al., 2014) confirmed this trend showing the appearance of five part span stall in the diffuser at the lower flow rate. Three stall cells developed from the hub up to less than 20% of the diffuser width, one from the shroud to the mid span and only one showed a stable full span configuration. Moreover the numerical analysis showed that vortices, originated in the first third of the impeller, evolved with periodic upward and downward phases in the same position. This sequence does not generate remarkable pressure pulsations and flow rate variation in each blade to blade channels (Pavesi G. et al., 2014).

The return channel front side close to the hub was occupied by the same vortex shown in Fig. 13. Moreover, when the diffuser was stalled the air, pumped out the hole number R4 on the return vane suction side, moved from the return channel outlet toward the U turn section, mixed with the flow in the front side and came back to the outlet (Fig. 15). Below $Q/Q_{Des} \approx 0.45$, that is for flow rate lower than the instability region, the periodic stall/back flow inside the diffuser disappeared. The bubbles path analyses only showed vortices with stochastically changing intensity and structure. In fig. 16 some of the vortexes are shown. The flow became more unstable and the disturbances both into the diffuser and in the return channels increased. Consistently the intensity of the overall pressure fluctuation measured at the exit of the impeller increased as shown in fig. 4.

CONCLUSIONS

Experimental analyses were carried out on a low specific speed pump-turbine operating at full and part load conditions on pump mode to study the characteristics and the development of the unsteady phenomena in saddle-instabilities region. Both the

pressure variation in time and frequency domains and high-speed flow visualizations were used to analyze the flow field in the instability region from 0.45 to 0.70 Q/Q_{Des} .

Two phenomena were highlighted coherently by both spectral and bispectral analysis of the pressure data. The fundamental sub frequency component $St_F \approx 0.6625$ was shown to be significant both in full and part load. Whereas, in the instability region, a second unsteady perturbation ($St_S \approx 0.335$) were detected in diffuser vane passage.

The results of high-speed flow visualizations confirmed that the fundamental frequency component ($St_F \approx 0.6625$) was due to the unsteady pattern in return channel, and showed the development of this unsteady structure at part the flow rate. The unsteady pattern presented a back flow region in the suction side of return vanes at the design flow rate. With the flow rate reduction, the reverse flow moved along the suction side towards the back side. The high-speed camera results highlighted that the second unsteady perturbation ($St_S \approx 0.335$) is coupled with an unsteady three-dimensional pattern into the diffuser vane channels.

The present study indicates that rotating stall frequency can be detected by spectral analysis of pressure time series just as well as by high-speed flow visualizations.

Despite the encouraging results, more work is still needed to better understand the hydrodynamics and to link the observed intensity or the intensity variation of the pressure pulsation with the characteristic head drop. Therefore in the future, study should focus on the dynamic characteristics of off-design conditions to connect the pressure drop with the energy carried out by the pressure fluctuations lost/dissipated. Moreover the instability appears to have different development and intensity changing the circumferential position of the diffuser with the return vanes.

REFERENCE

- [1] Henry J M, Houdeline J B, Ruiz S, Kunz T (2012) How reversible pump-turbines can support grid variability - The variable speed approach. HYDRO 2012 Innovative Approaches to Global Challenges, 29-31 October 2012, Bilbao, Spain.

- [2] Yuekun Sun, Zhigang Zuo, Shuhong Liu, Jintao Liu, and Yulin Wu (2014) Distribution of Pressure Fluctuations in a Prototype Pump Turbine at Pump Mode, *Advances in Mechanical Engineering* Volume 2014, Article ID 923937.
- [3] Hui Sun; Ruofu Xiao; Weichao Liu; Fujun Wang (2013) Analysis of S Characteristics and Pressure Pulsations in a Pump-Turbine With Misaligned Guide Vanes, *J. Fluids Eng.*. 2013; 135(5), 051101-051101-6. FE-12-1122, doi: 10.1115/1.4023647
- [4] Li, W (2012) Numerical investigation of pump-turbines with different blades at pump conditions, *Journal of advanced manufacturing systems* [0219-6867] vol:11(2), pp 143-153.
- [5] Rodriguez C G, Mateos-Prieto B, and Egusquiza E Monitoring of Rotor-Stator Interaction in Pump-Turbine Using Vibrations Measured with On-Board Sensors Rotating with Shaft, *Shock and Vibration*, Volume 2014 (2014), Article ID 276796.
- [6] González J, Fernández J, Blanco E, Santolaria C (2002) Numerical Simulation of the Dynamic Effects Due to Impeller-Volute Interaction in a Centrifugal Pump. *J. Fluids Eng.*, 12, pp. 348–355, DOI: 10.1115/1.1457452.
- [7] Cavazzini G, Pavesi G, Ardizzon G, Dupont P, Coudert S, Caignaert G, Bois G (2009) Analysis of the rotor-stator interaction in a radial flow pump. *La Houille Blanche, Revue Internationale de l'eau*, 2009, 5, pp. 141–151, DOI 10.1051/lhb/2009067
- [8] Sano T, Yoshida Y, Tsujimoto Y, Nakamura Y, Matsushima T (2002) Numerical Study of Rotating Stall in a pump vaned diffuser, *J. Fluids Eng.*, vol. 124, pp. 363-370
- [9] Perdesen N, Larsen PS, Jacobsen CB (2003) Flow in a Centrifugal Pump Impeller at Design and Off-Design Conditions—Part I: Particle Image Velocimetry (PIV) and Laser Doppler Velocimetry (LDV) Measurements. *J. Fluids Eng.*, vol. 125, pp. 61-72, DOI: 10.1115/1.1524585
- [10] Hong SS, Kang SH (2004) Flow at the centrifugal pump impeller exit with the circumferential distortion of the outlet static pressure. *J. Fluids Eng.*, 126(1), pp. 81–86, DOI: 10.1115/1.1637630
- [11] Majidi K (2005) Numerical study of unsteady flow in a centrifugal pump. *J. Turbomach*, 127(2), pp. 363–371, DOI: 10.1115/1.1776587
- [12] Guo S, Maruta Y. (2005) Experimental investigations on pressure fluctuations and vibration of the impeller in a centrifugal pump with vaned diffusers. *JSME Int. J., Ser. B*, 48(1), pp. 136–143.

- [13] Rodriguez CG, Egusquiza E, and Santos IF (2007) Frequencies in the vibration induced by the rotor stator interaction in a centrifugal pump turbine. *J. Fluids Eng.*, 129(11), pp. 1428–1435, DOI: 10.1115/1.2786489
- [14] Pavesi G, Cavazzini G, Ardizzon G. (2008) Time–frequency characterization of the unsteady phenomena in a centrifugal pump. *Int. J. Heat Fluid FL*, 29, pp. 1527–1540, DOI: 10.1016/j.ijheatfluidflow.2008.06.008
- [15] Gülich JF (2010) *Centrifugal pumps* 2nd edn. Springer Berlin Heidelberg New York
- [16] Cavazzini G, Pavesi G, Ardizzon G (2011) Pressure instabilities in a vaned centrifugal pump, *Proceedings of the Institution of Mechanical Engineers, Part A: Journal of Power and Energy*, 225(7), pp. 930-939
- [17] Gentner Ch, Sallaberger M, Widmer Ch, Barun O, Staubli T (2012) Analysis of unstable operation of pump turbines and how to avoid it, *HYDRO 2012 Innovative Approaches to Global Challenges*, 29-31 October 2012, Bilbao, Spain
- [18] Torrence C, Compo G, (1998) A practical guide to wavelet analysis. *Bull. Am. Meteorol. Soc.* 79 (1), pp. 61–78.
- [19] Farge M (1992) Wavelet transforms and their application to turbulence. *Annu. Rev. Fluid Mech.* 24, pp. 395–457.
- [20] Yang J, Pavesi G, Cavazzini G, Yuan S (2013) Numerical characterization of pressure instabilities in a vaned centrifugal pump under part load condition. *IOP Conf. Ser.: Mater. Sci. .Eng.* 52 0022044, 6th International Conference on Pumps and Fans with Compressors and Wind Turbines (ICPF2013), DOI: 10.1088/1757-899X/52/2/022044
- [21] Rosenblatt M, Van Ness JW (1965) Estimation of the Bispectrum. *Ann. Math. Stat.*, vol. 36, pp. 1120-1136
- [22] Akin O, Rockwell DO (1994) Actively controlled radial flow pumping system: manipulation of spectral content of wakes and wake-blade interactions. *J. Fluids Eng.* 116, pp. 528–537.
- [23] Pavesi G., Cavazzini G., Jun Yang, Ardizzon G. (2014) Flow Phenomena Related to the Unstable Energy-Discharge Characteristic of a Pump-Turbine in Pump Mode 15th International Symposium on Transport Phenomena and Dynamics of Rotating Machinery, ISROMAC-15 February 24 - 28, 2014, Honolulu, HI, USA
- [24] Minemura, K., Murakami, M. (1980): A Theoretical Study on Air Bubble Motion in a Centrifugal Pump Impeller, *Proc. ASME/JSME Fluid Eng. Conf.*, Fed-Vol. 102, pp. 446-455)

- [25] Pavesi G., Cavazzini G., Ardizzon G. (2008) Time-frequency characterization of rotating instabilities in a centrifugal pump with a vaned diffuser, *International Journal of rotating Machinery*, Vol. 2008 , DOI: 10.1155/2008/202179

- [26] Li Deyou, wang Hongjie, Xiang Gaoming, Gong Ruzhi, Wei Xianzhu, Liu Zhansheng (2015) Unsteady simulation and Analysis for hump characteristics of a pump turbine model, *Renewable Energy*, 77 (2015), pp. 32-42, DOI: 10.1016/j.renene.2014.12.004

FUNDING

Project supported by the University of Padova (No. CPDA130025/13), National Natural Science Foundation of China (Grant No. 51409123) China Postdoctoral Science Foundation funded project (Grant No. 2014M560402)

NOMENCLATURE

BPF	Blade Passage Frequency, Hz
f	frequency, Hz
g	acceleration due to gravity, m/s^{-2}
h	head, m
n	rotational speed of the impeller, 600 rpm
$n_s = n \frac{Q^{0.5}}{h^{0.75}}$	specific speed, $m^{0.75} s^{-1.5}$
Q	flow rate, $m^3 s^{-1}$
p	pressure [Pa]
$St = \frac{f}{BPF}$	Strouhal number
Δp	static pressure increase between impeller inlet and outlet
$\omega_s = \frac{\pi n}{30} \frac{Q^{0.5}}{(gh)^{0.75}}$	dimensionless specific speed

Subscript

Des	design
-------	--------

Figure Captions List

- Fig. 1 3D scheme of the tested configuration.
- Fig. 2 Diffuser reference position ($\lambda=0^\circ$) and tested configuration ($\lambda=8^\circ$) with the distribution of monitor points.
- Fig. 3 Experimental pump characteristics and saddle-type instabilities region
- Fig. 4 Mean pressure variation at the exit of the impeller and impeller static pressure increase with band of oscillation measured at impeller outlet versus the flow.
- Fig. 5 Power spectrum of pressure measured by the pressure transducers D5, D6, D11 and D12 in the diffuser vane.
- Fig. 6 Bispectrum of pressure measured by the pressure transducer D6 in the diffuser vane for $0.59 Q_{Des}$ (a), $0.60 Q_{Des}$ (b)
- Fig. 7 Wavelet magnitude $|W_n|$ of the pressure signal (transducer D6) in the diffuser vane for $0.62 Q_{Des}$ (a), $0.60 Q_{Des}$ (b) and $0.59 Q_{Des}$ (c).
- Fig. 8 Cross wavelet magnitude $|W_n|$ of the pressure signal in the diffuser vane for $0.60 Q_{Des}$ and $0.59 Q_{Des}$
- Fig. 9 Frames obtained by high speed camera at design flow rate in the diffuser and return channel at design flow rate
- Fig. 10 Frames obtained by high speed camera in the diffuser at flow rates from 0.9 to $0.8Q/Q_{Des}$

- Fig. 11 Sketch map of the bubbles tracks in diffuser.
- Fig. 12 Frames sequence obtained by high speed camera at $0.63 Q/Q_{Des}$ in the diffuser.
- Fig. 13 Frames obtained by high speed camera at $0.63 Q/Q_{Des}$ in the return channel
- Fig. 14 Frames sequence obtained by high speed camera at $0.59 Q/Q_{Des}$ in the diffuser.
- Fig. 15 Frames obtained by high speed camera at $0.59 Q/Q_{Des}$ in the return channel.
- Fig. 16 Frames sequence obtained by high speed camera at $0.35 Q/Q_{Des}$ in the diffuser.

Table Caption List

- Table 1 Geometry characteristics and performance parameters of the tested pump-turbine.
- Table 2 Identified independent frequency components.

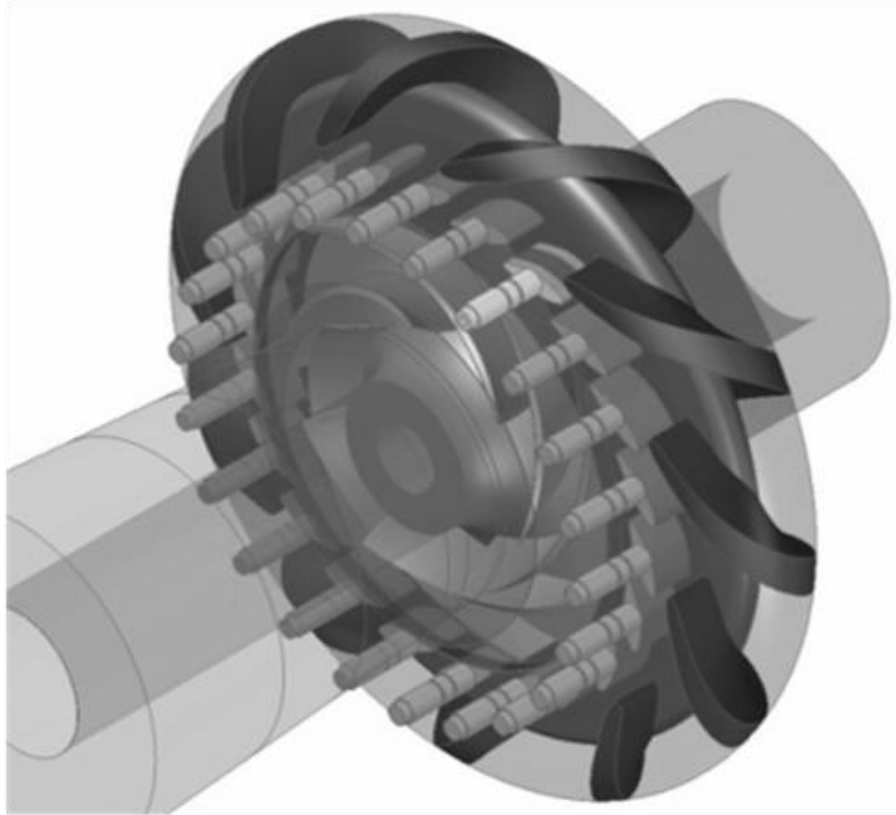


Fig. 1 3D scheme of the tested configuration.

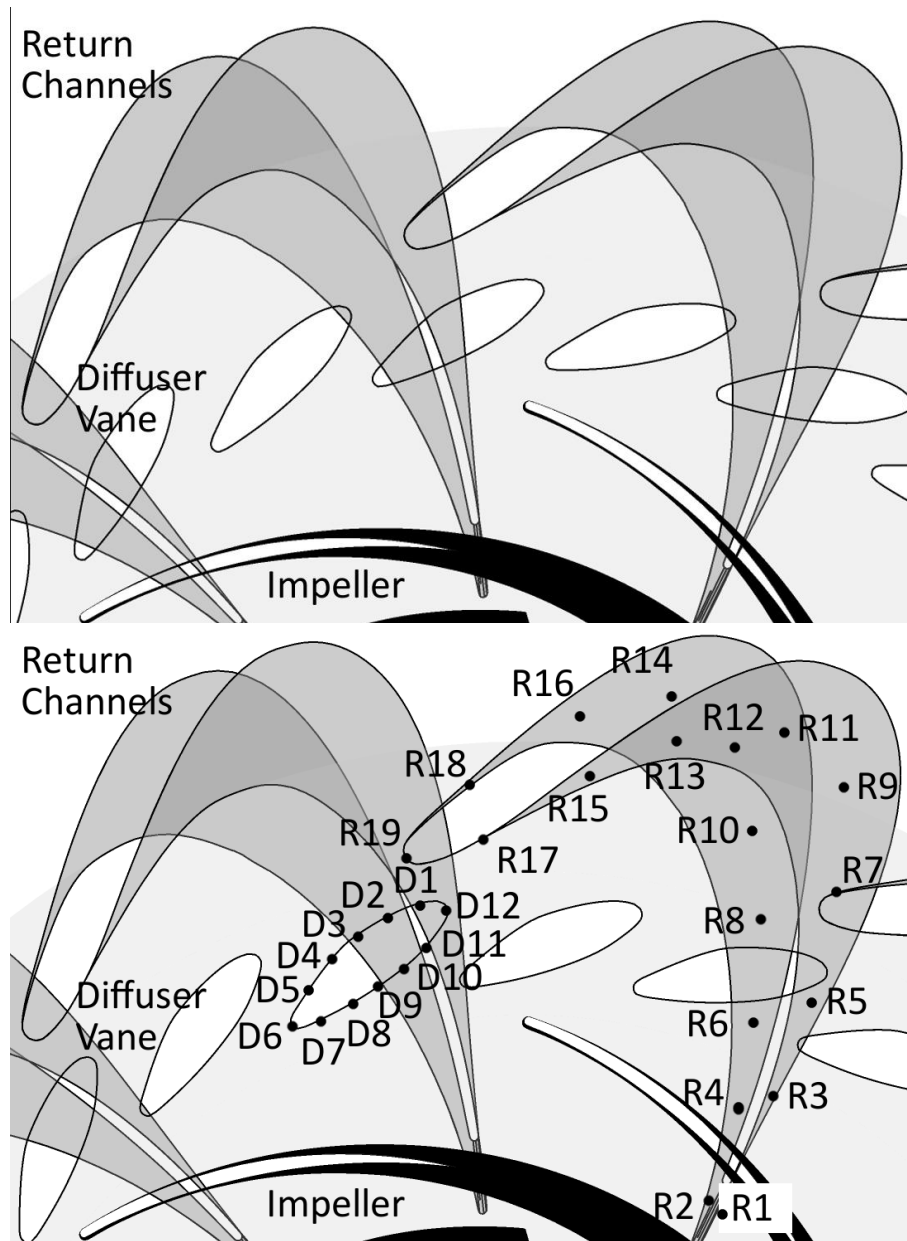


Fig. 2 Diffuser reference position ($\lambda=0^\circ$) and tested configuration ($\lambda=8^\circ$) with the distribution of monitor points.

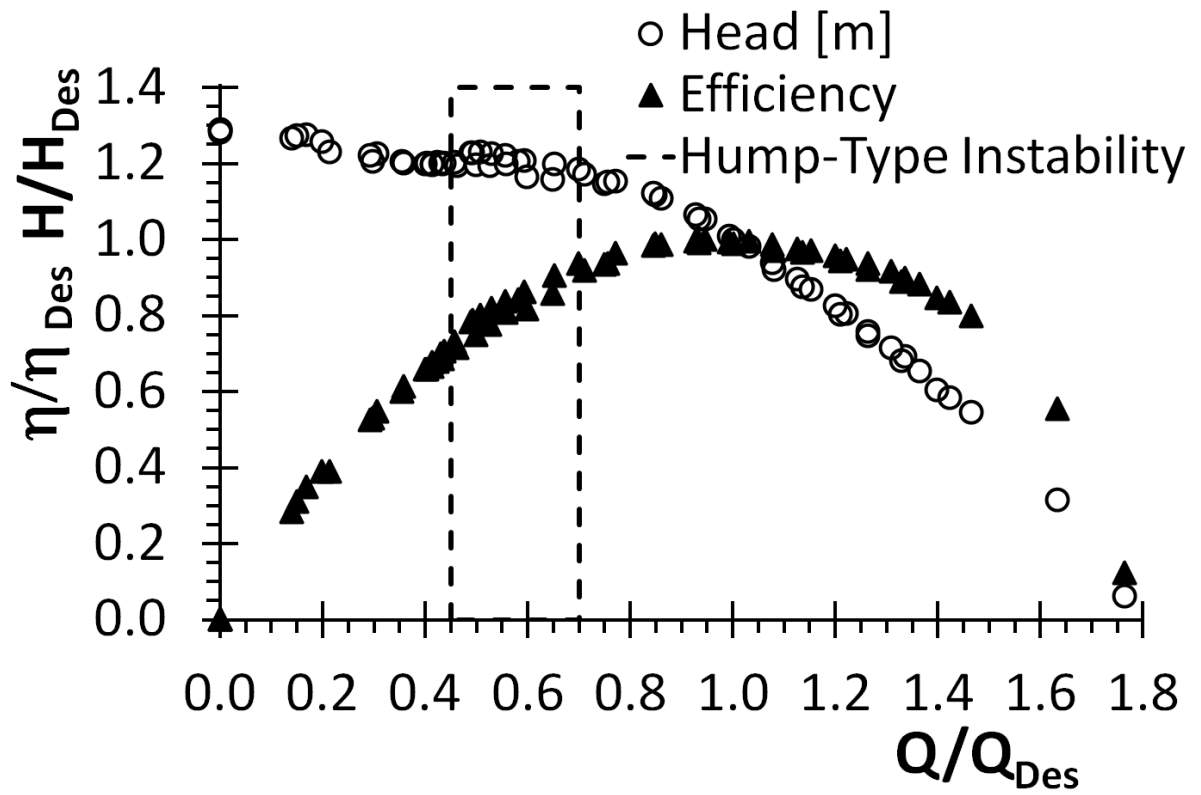


Fig. 3 Experimental pump characteristics and saddle-type instabilities region

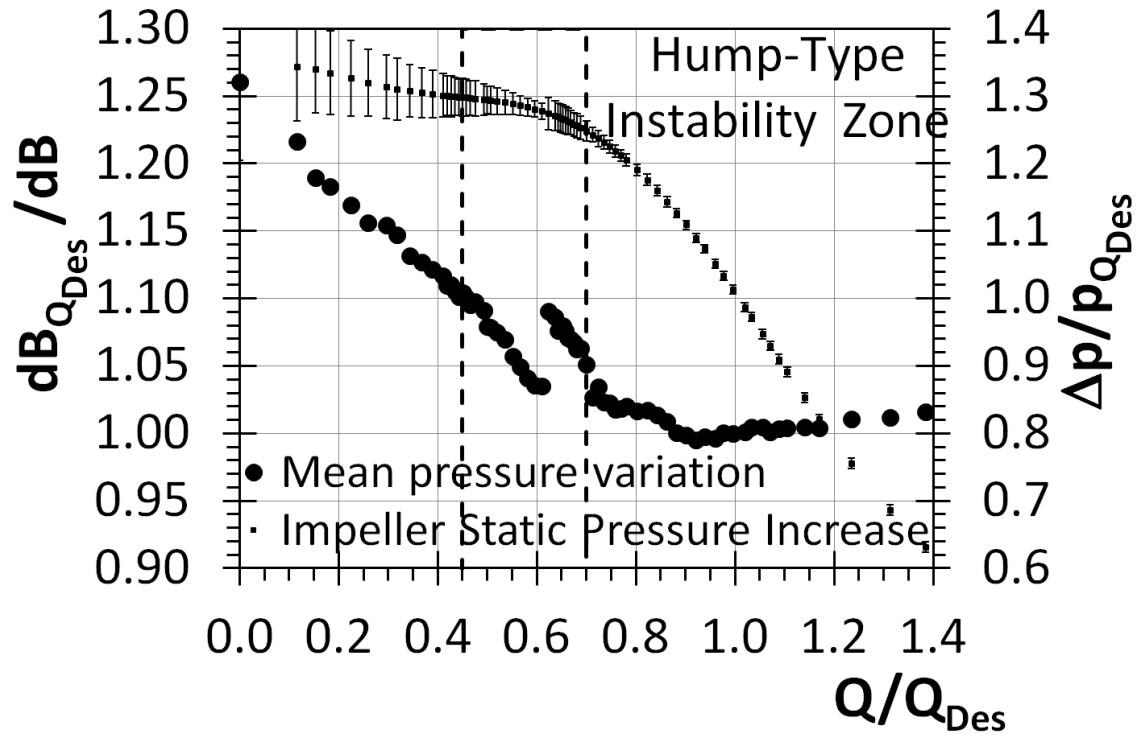
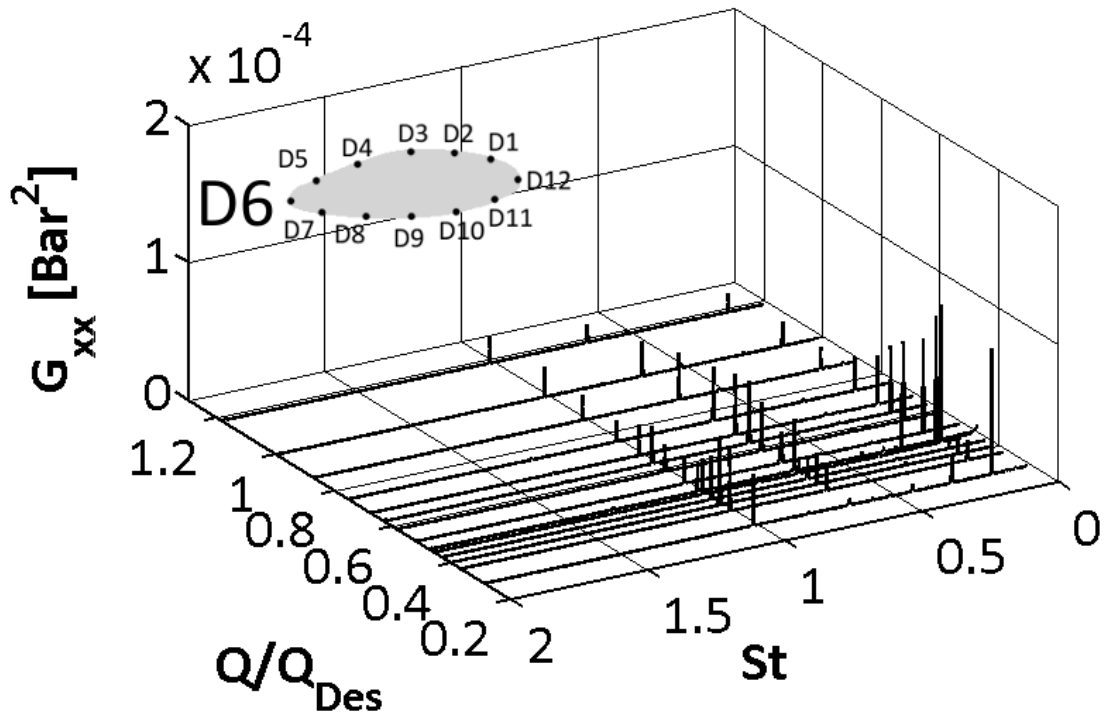
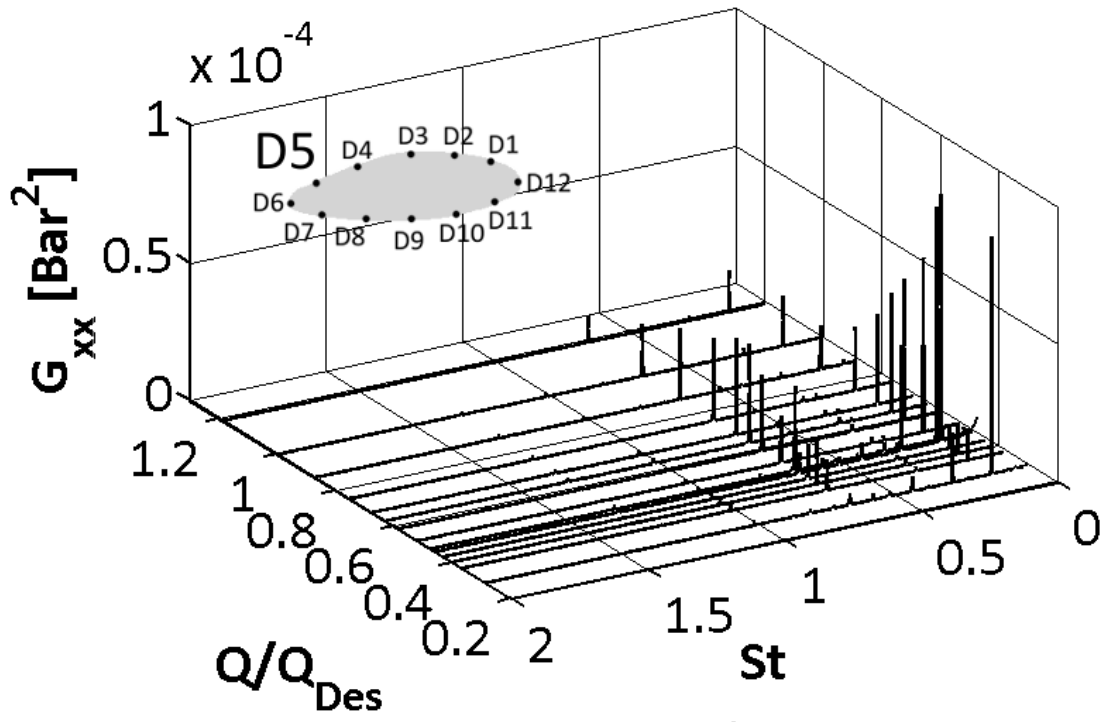


Fig. 4 Mean pressure variation at the exit of the impeller and impeller static pressure increase with band of oscillation measured at impeller outlet versus the flow.



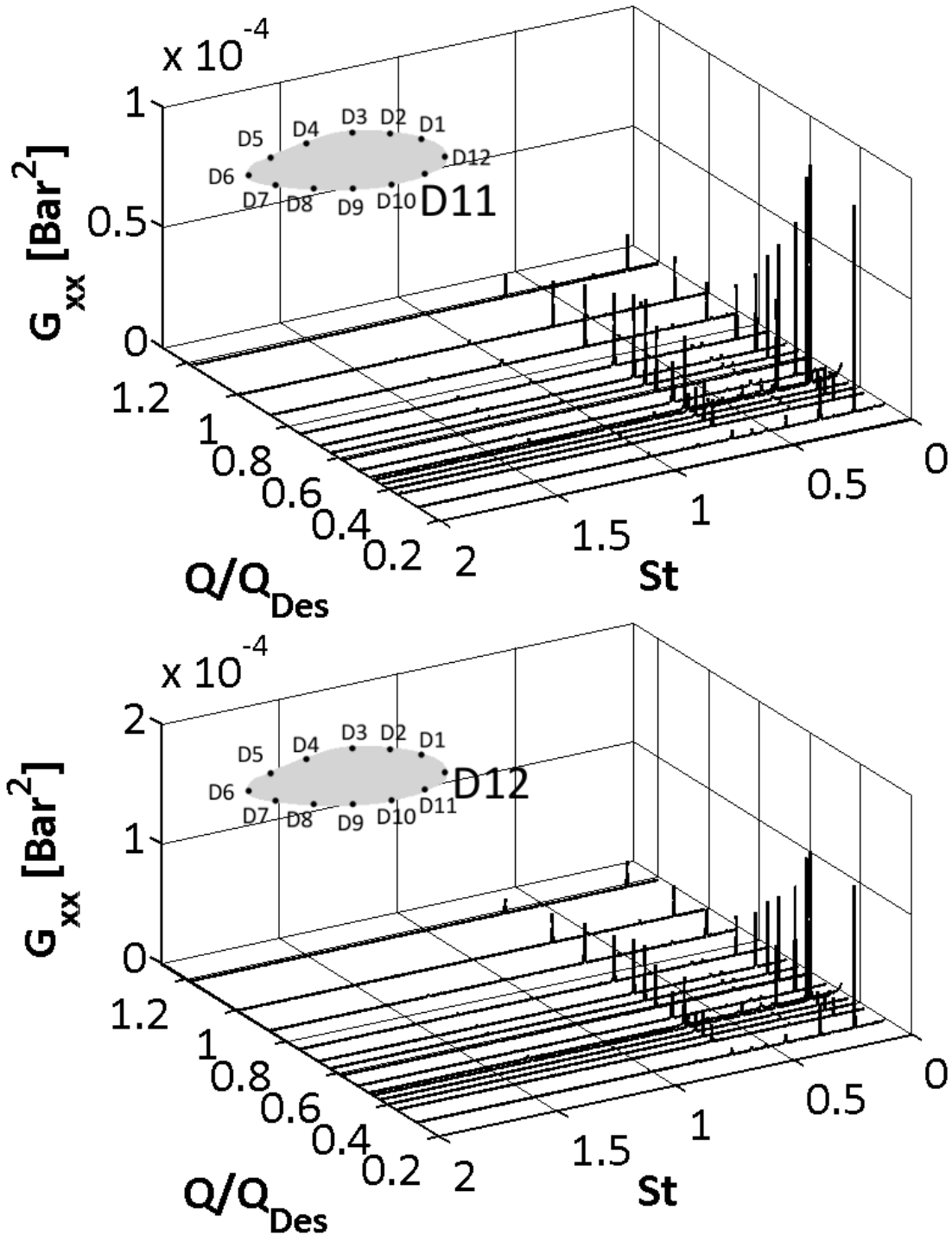
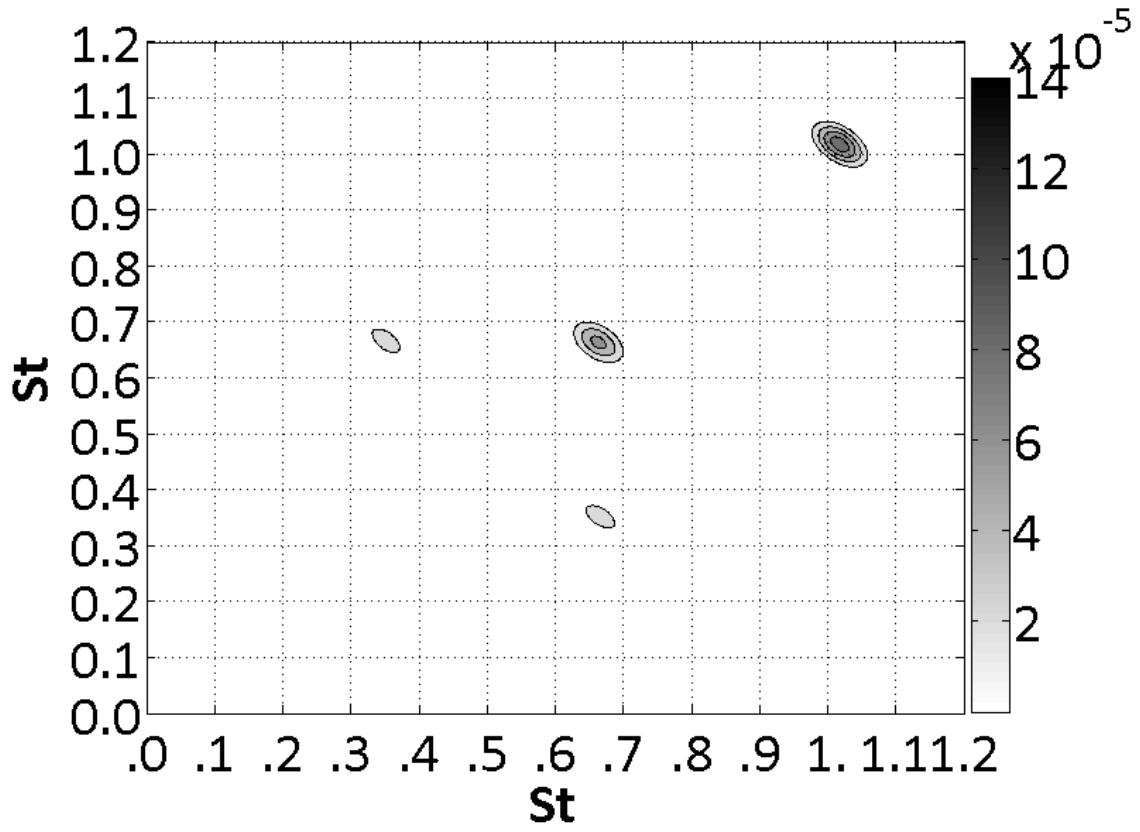
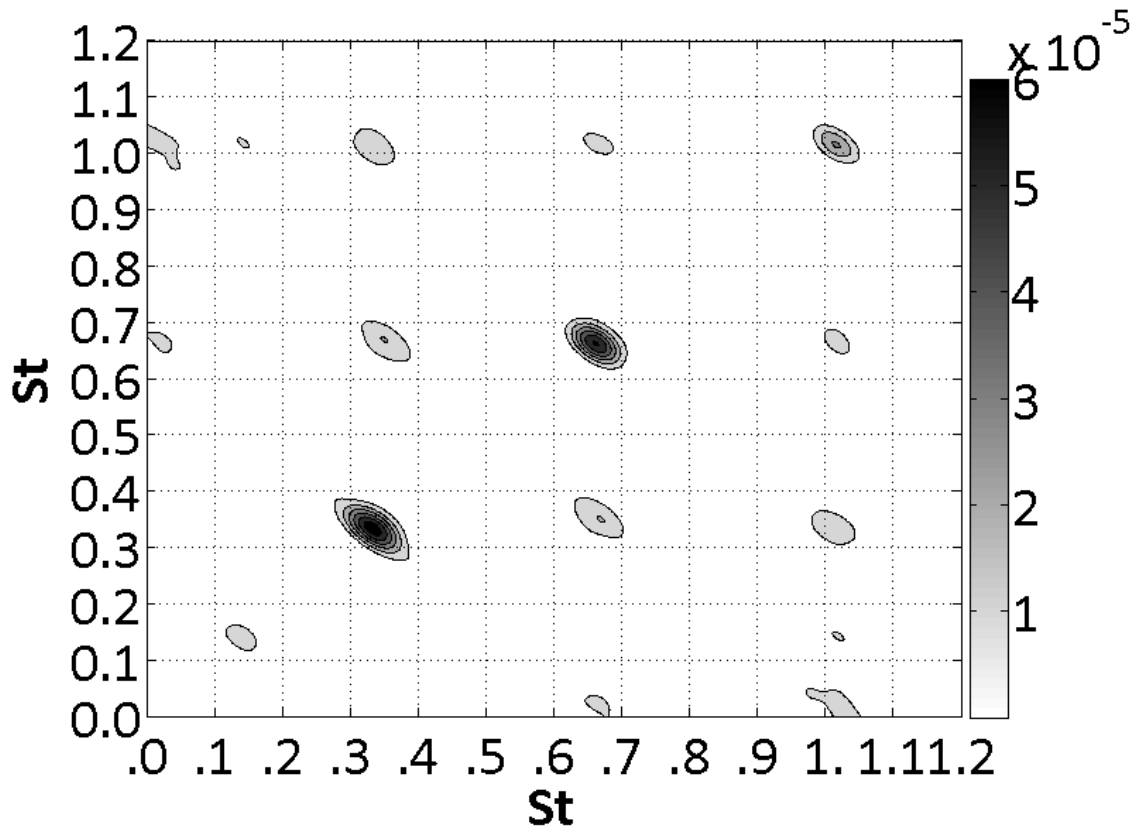


Fig. 5 Power spectrum of pressure measured by the pressure transducers D5, D6, D11 and D12 in the diffuser vane.

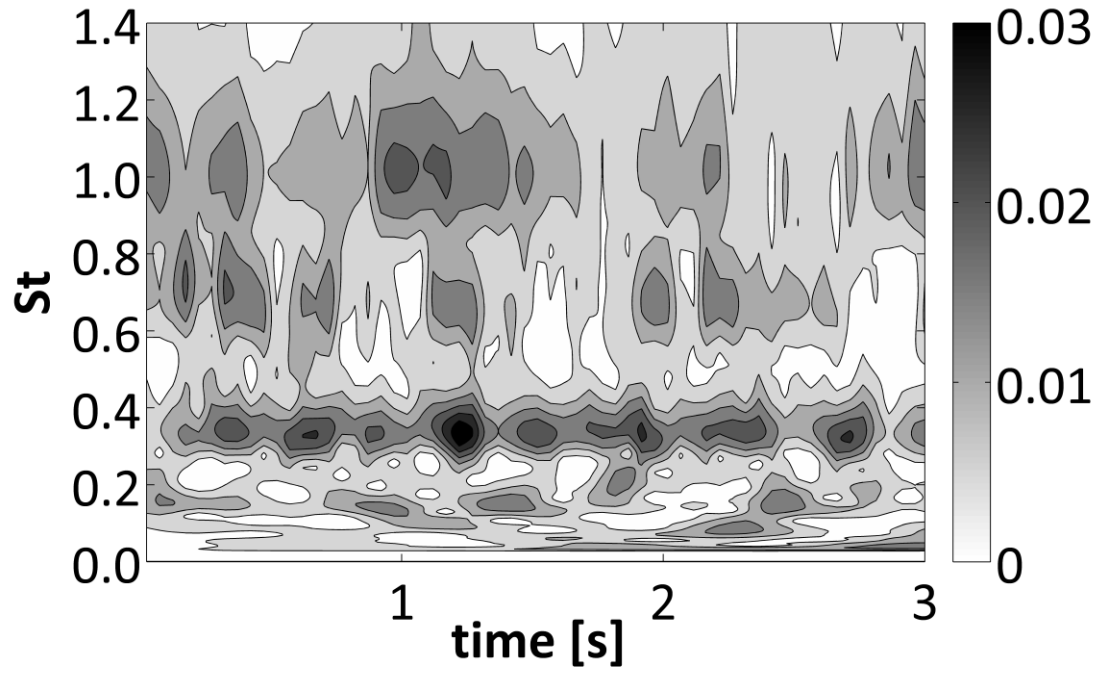


a)

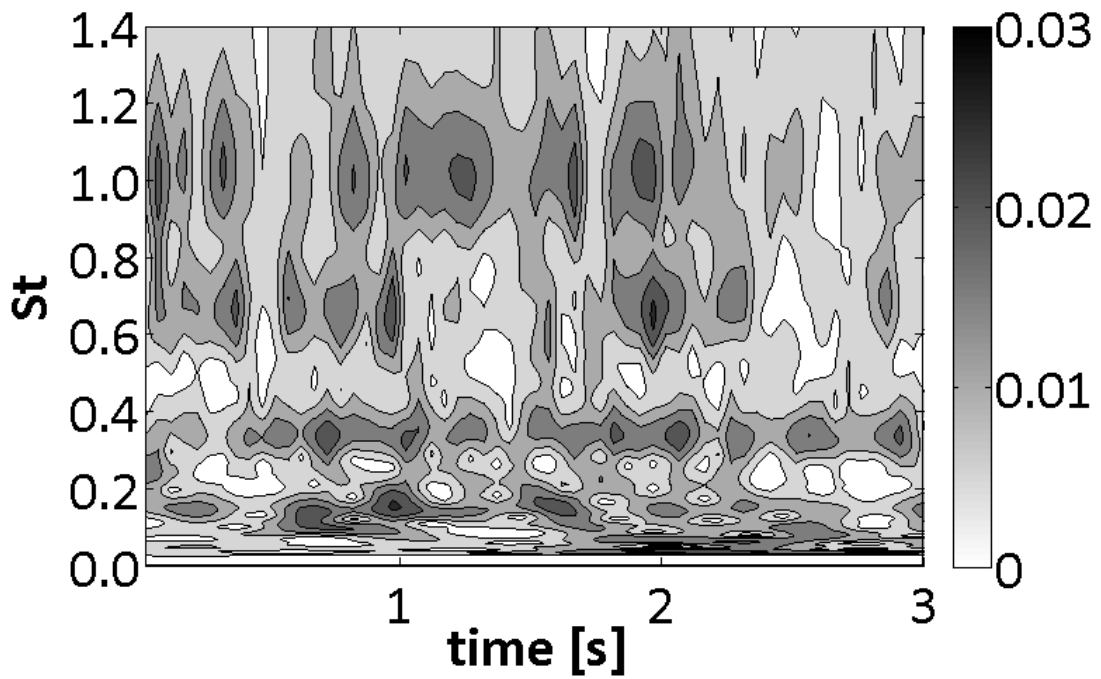


b)

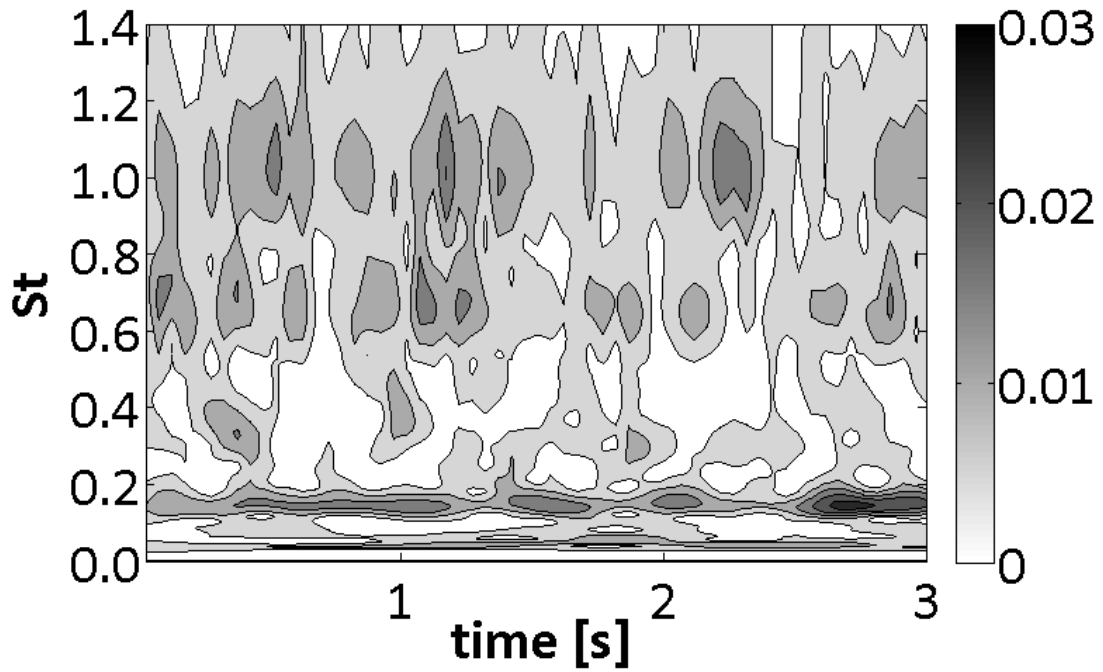
Fig. 6 Bispectrum of pressure measured by the pressure transducer D6 in the diffuser vane for $0.59 Q_{Des}$ (a), $0.60 Q_{Des}$ (b)



(a)



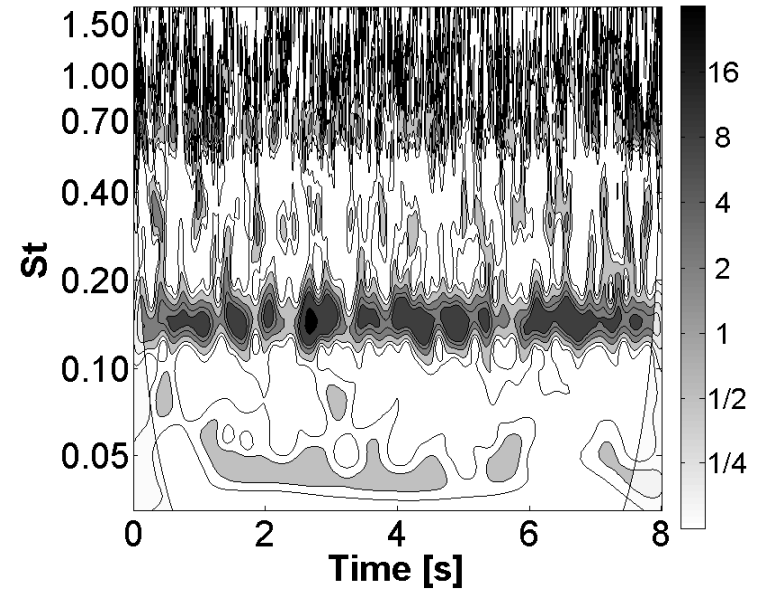
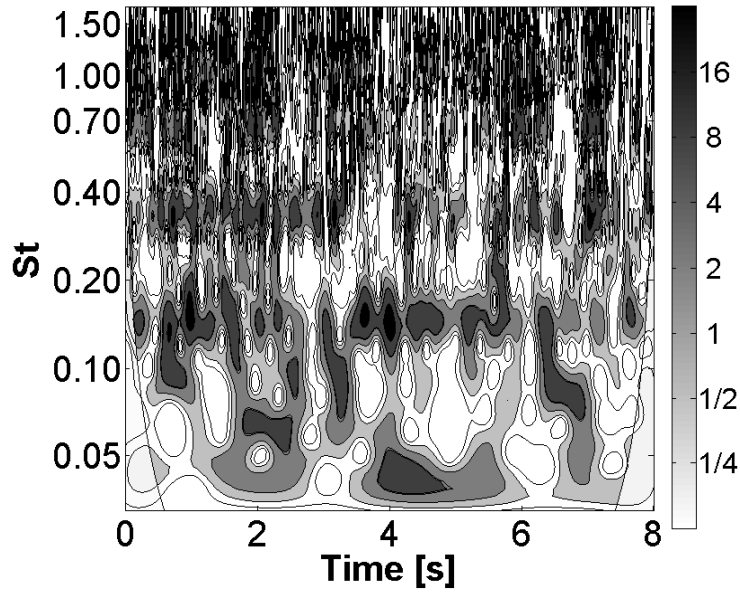
(b)



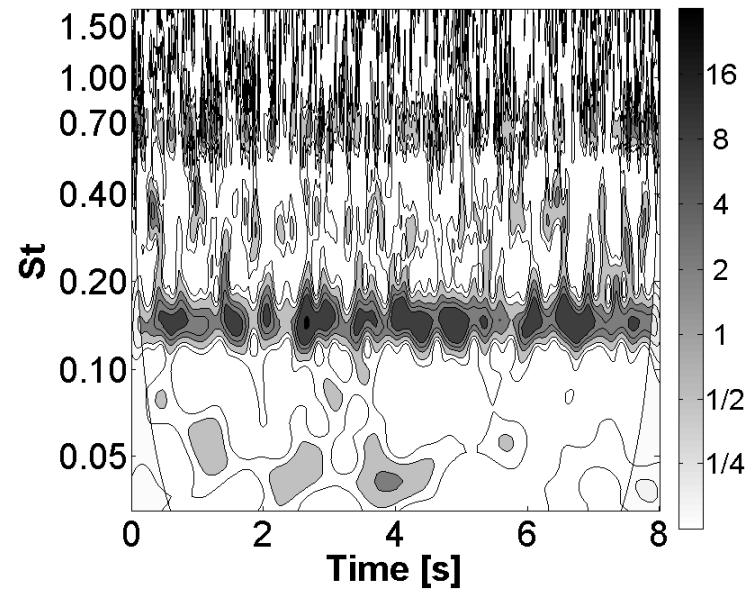
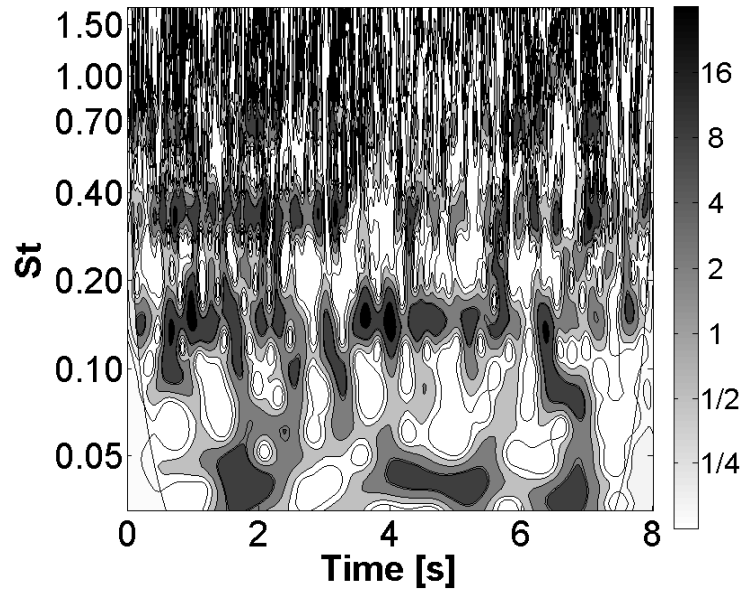
(c)

Fig.7 Wavelet magnitude $|W_n|$ of the pressure signal (transducer n° D6) in the diffuser vane for $0.62 Q_{Des}$ (a), $0.60 Q_{Des}$ (b) and $0.59 Q_{Des}$ (c).

Transducers n° D5-D6



Transducers n° D11-D12



(a) $0.60 Q/Q_{Des}$

(b) $0.59 Q/Q_{Des}$

Fig. 8 Cross wavelet magnitude $|W_n|$ of the pressure signal in the diffuser vane for $0.60 Q_{Des}$ and $0.59 Q_{Des}$

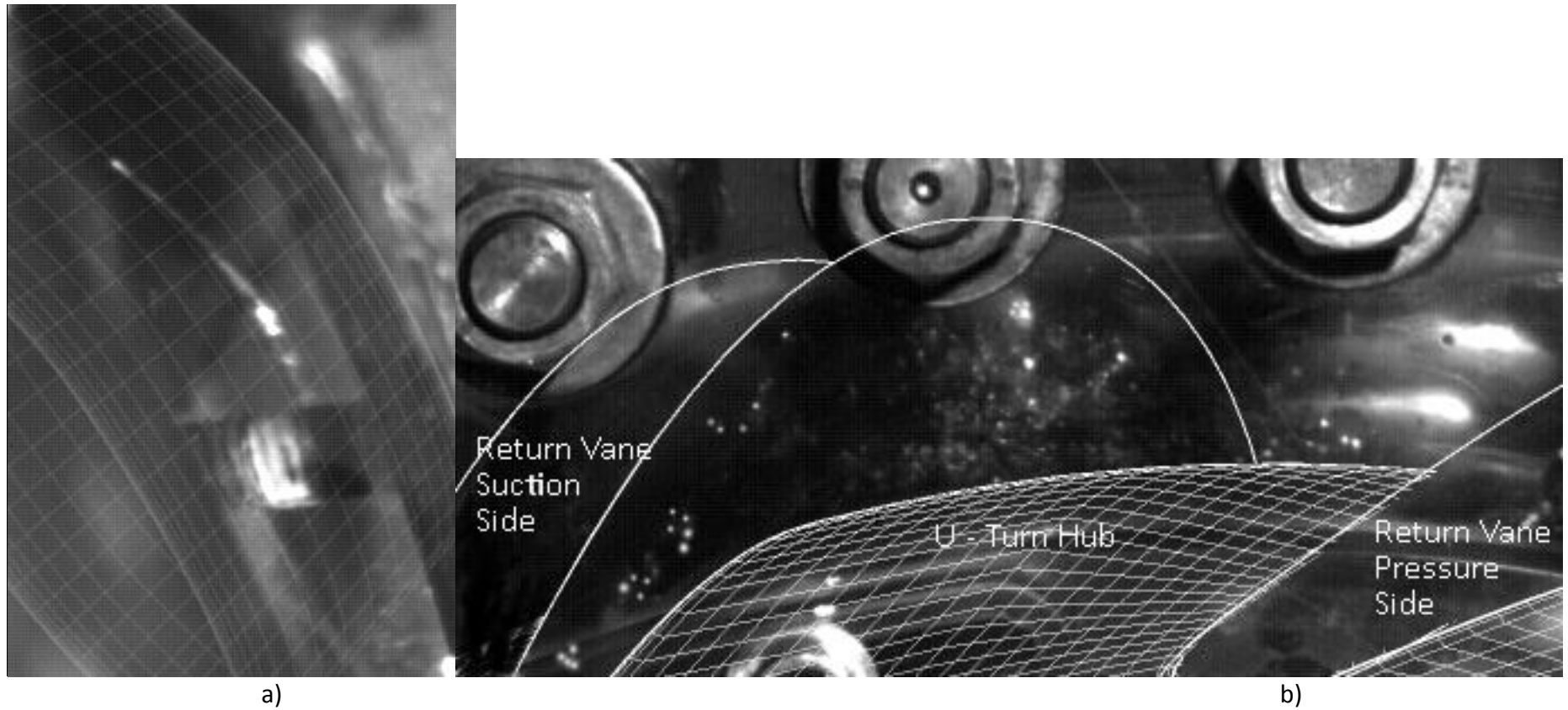


Fig. 9 Frames obtained by high speed camera at design flow rate in the diffuser and return channel at design flow rate

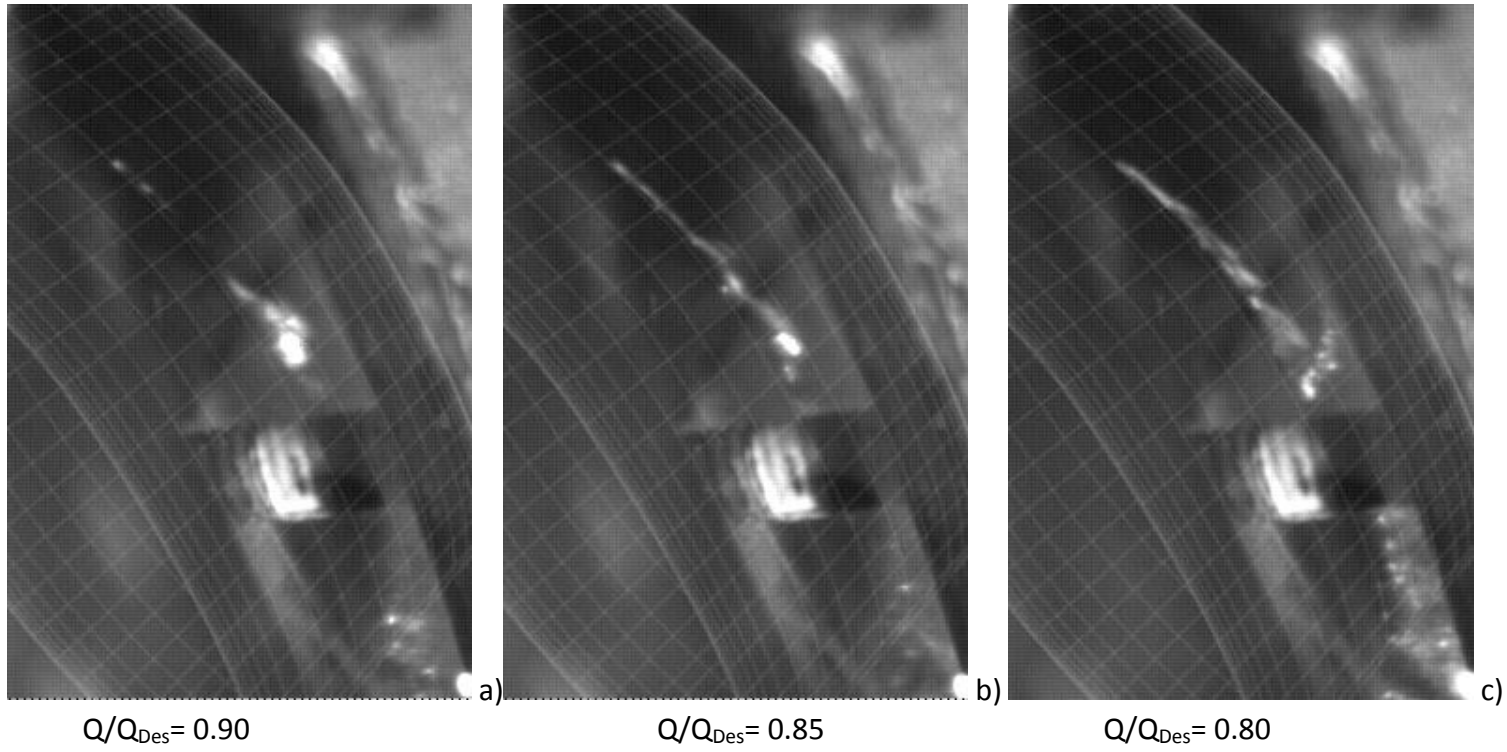


Fig. 10 Frames obtained by high speed camera in the diffuser at flow rates from 0.9 to 0.8 Q/Q_{Des}

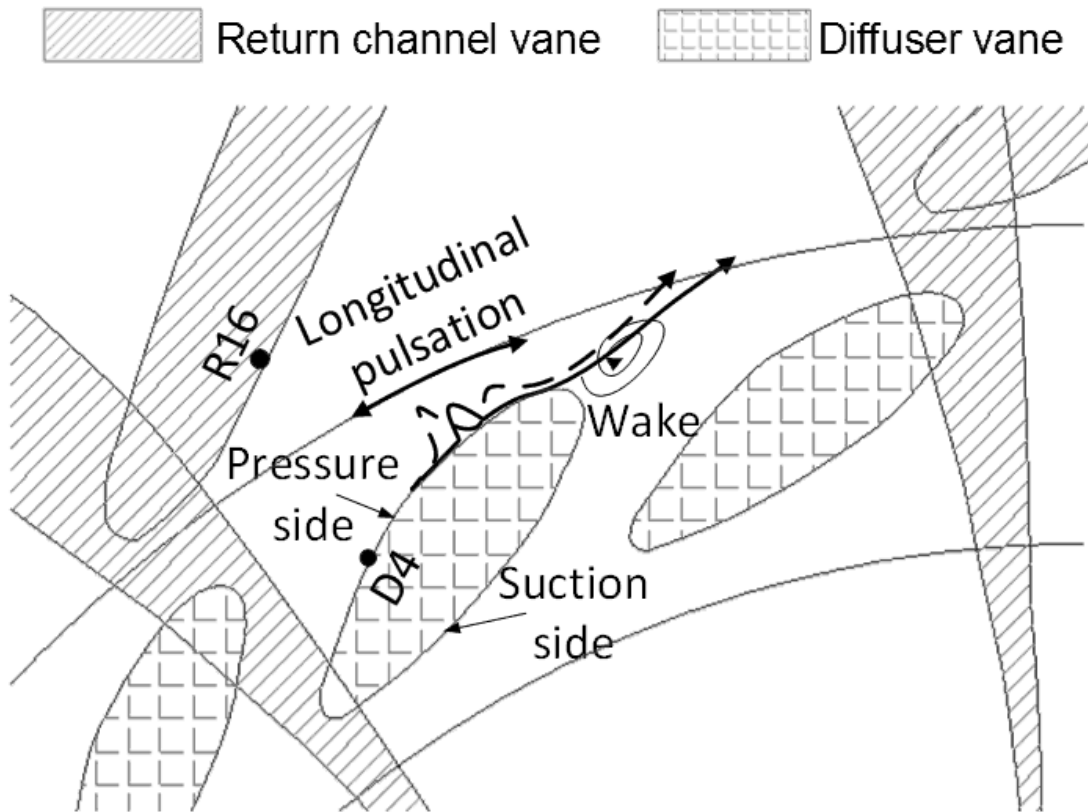


Fig.11 Sketch map of the bubbles tracks in diffuser.

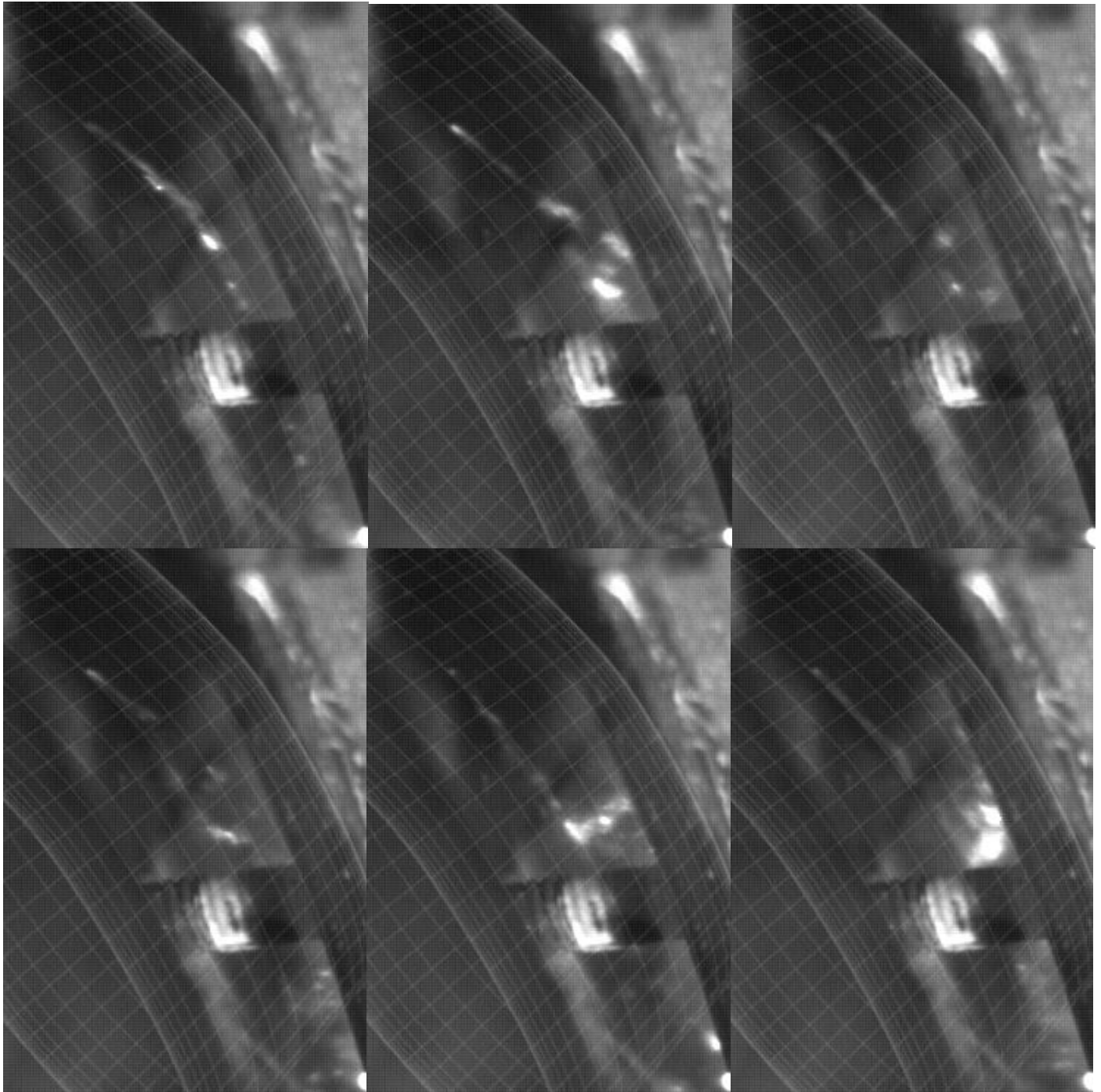
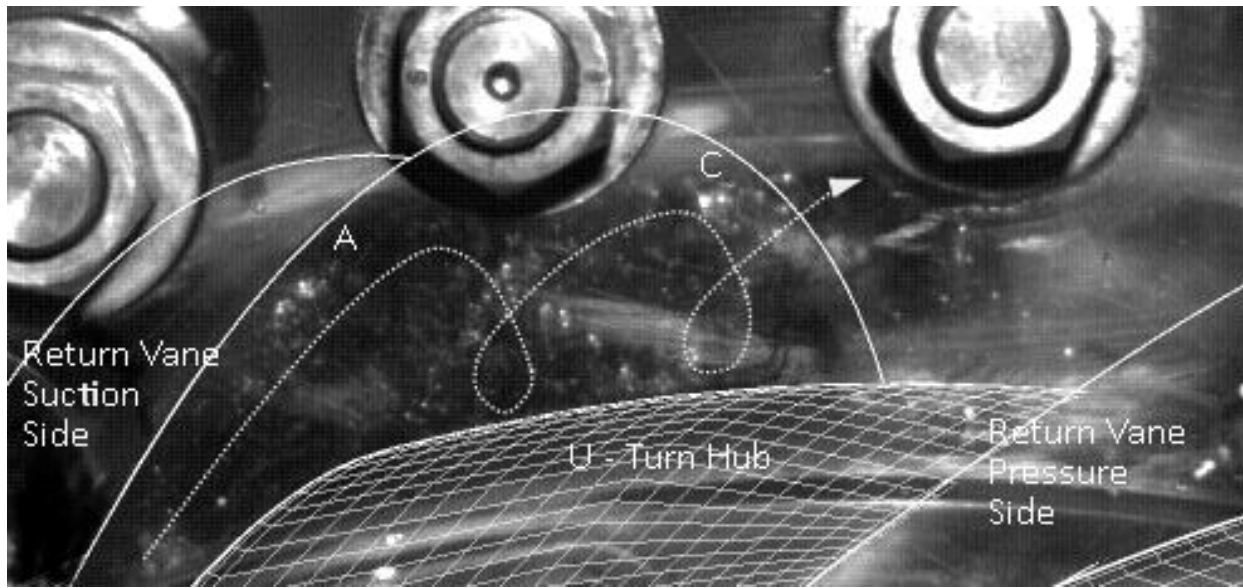
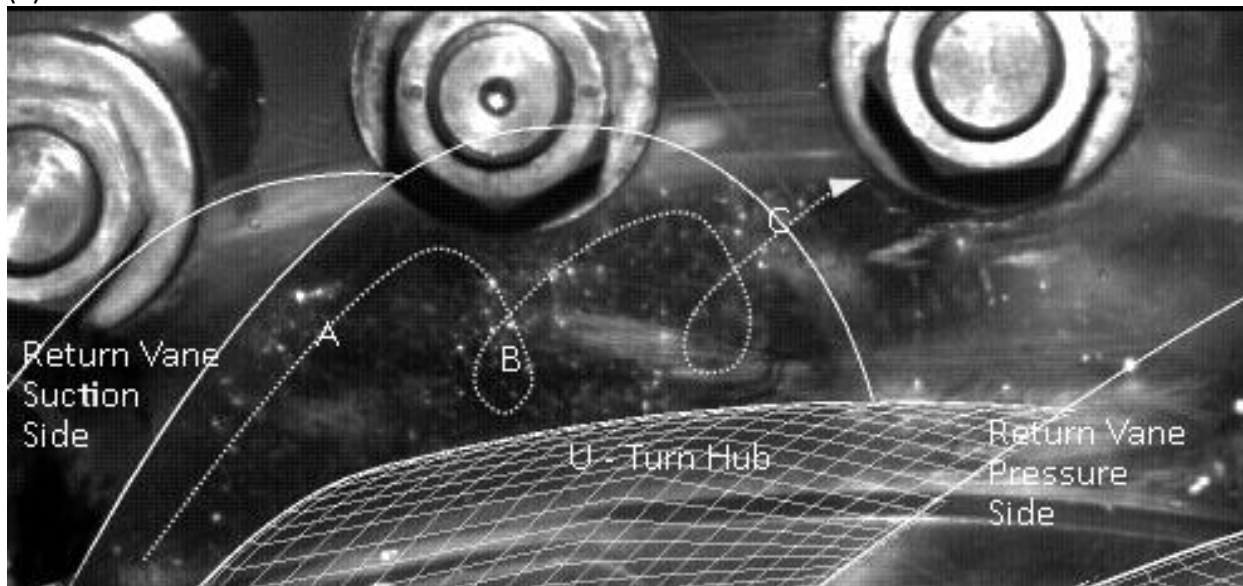


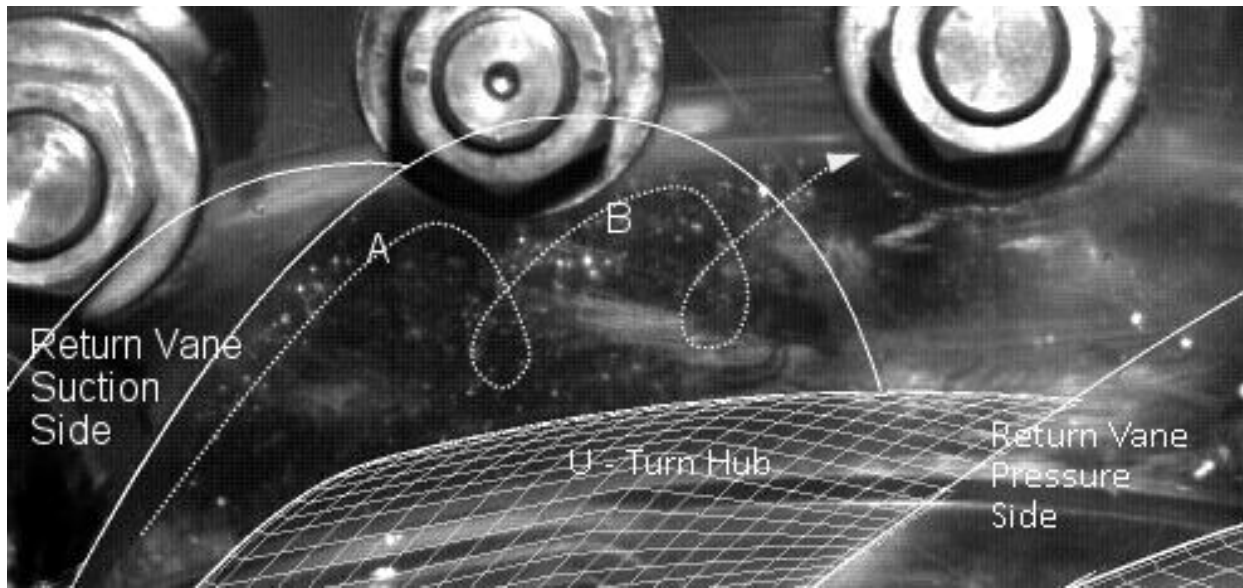
Fig. 12 Frames sequence obtained by high speed camera at $0.63 Q/Q_{Des}$ in the diffuser.



(a)



(b)



(c)

Fig. 13 Frames obtained by high speed camera at $0.63 Q/Q_{Des}$ in the return channel

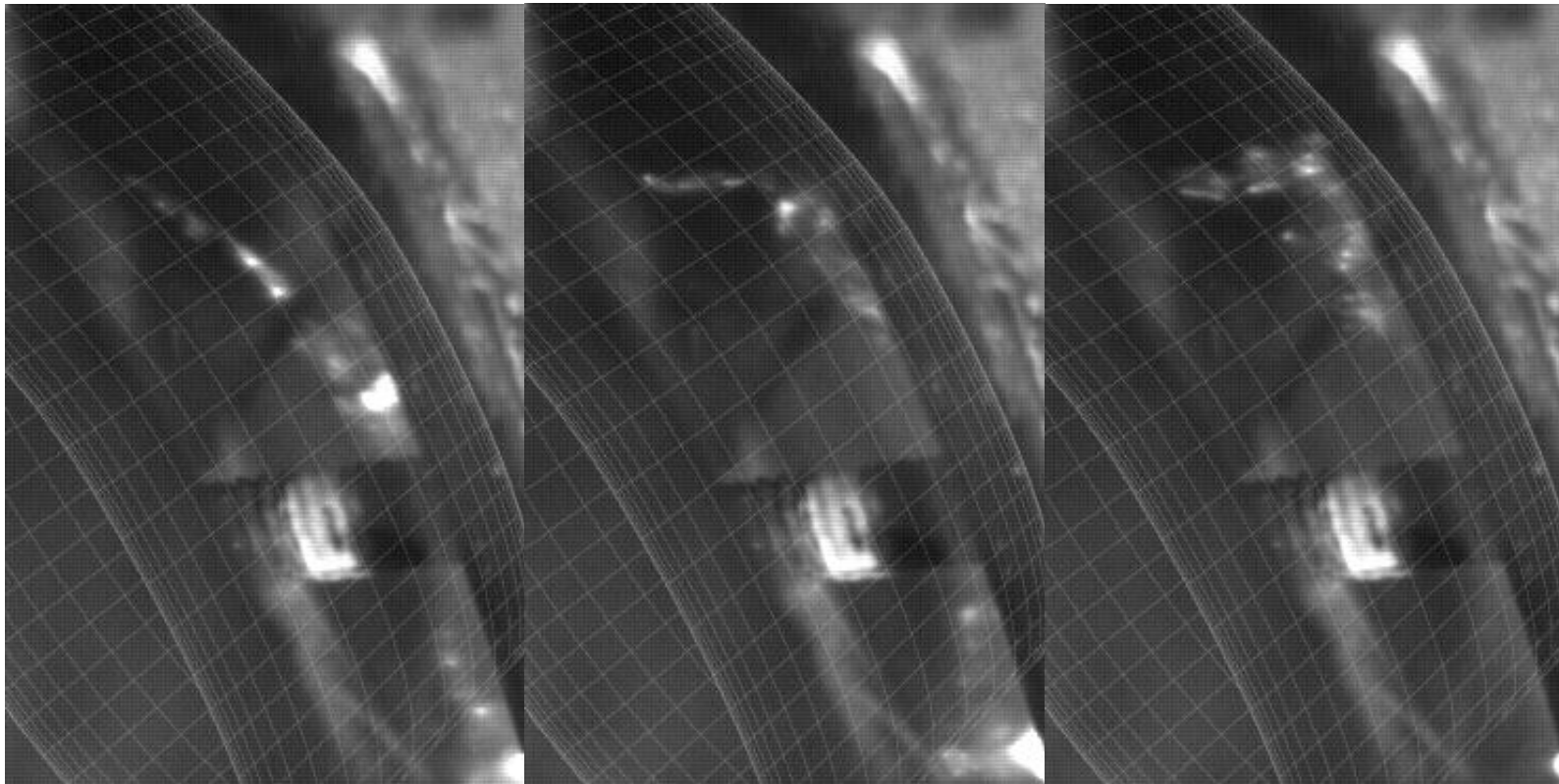
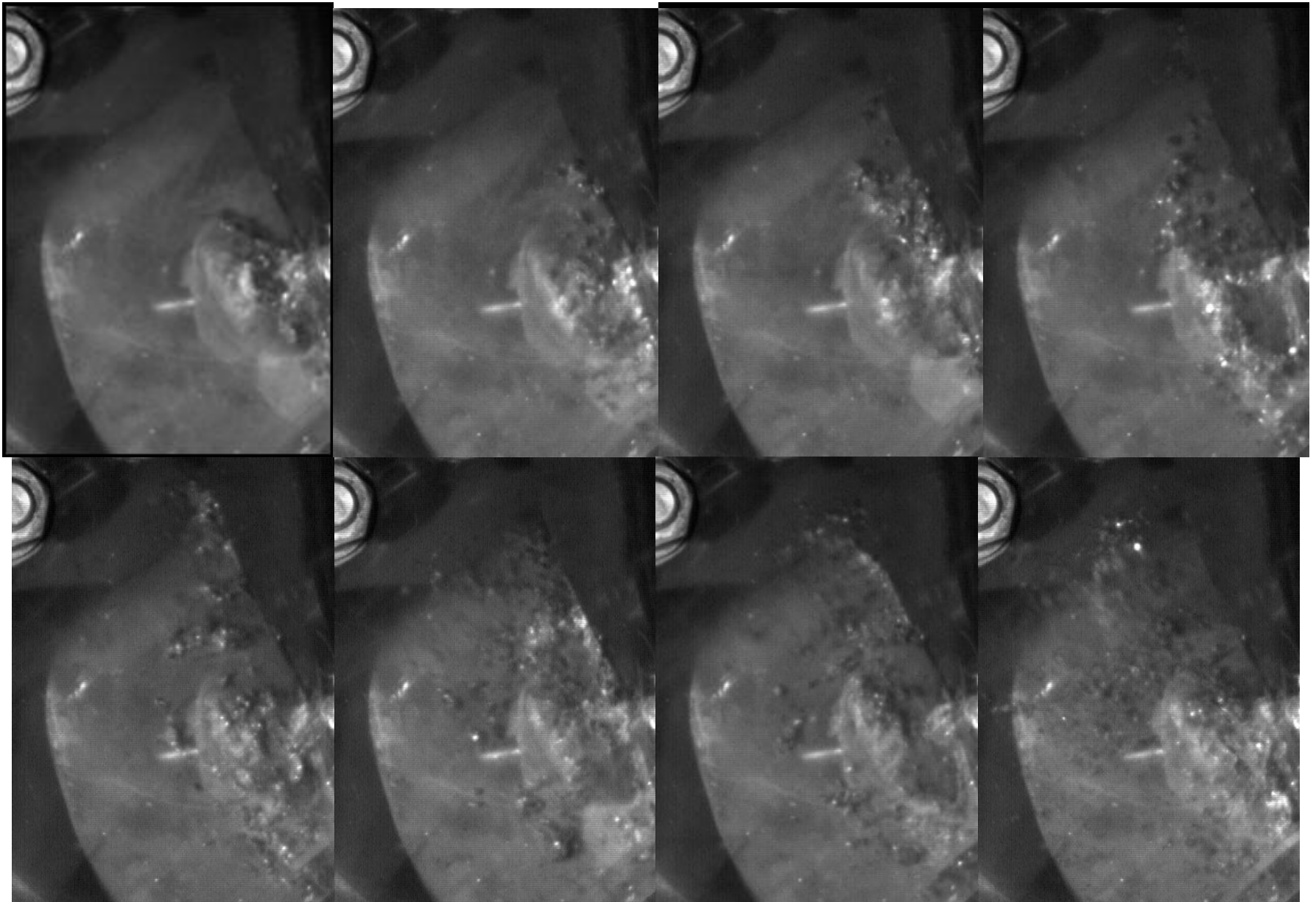


Fig. 14 Frames sequence obtained by high speed camera at $0.59 Q/Q_{Des}$ in the diffuser.



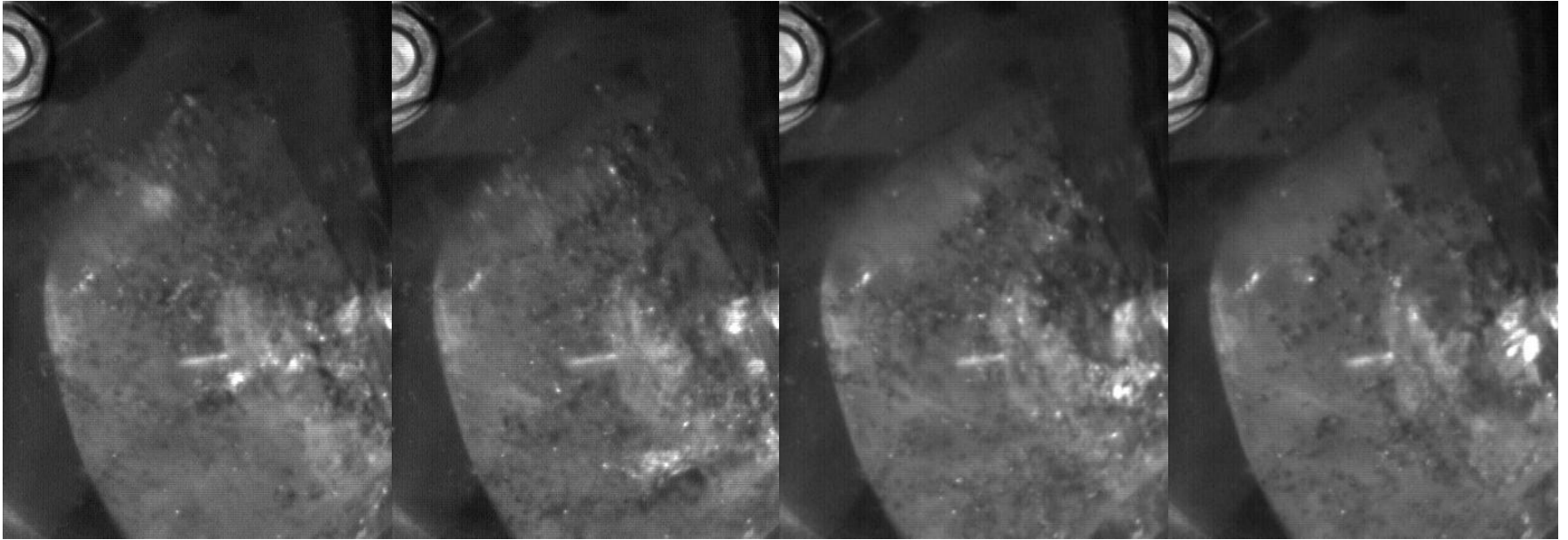


Fig. 15 Frames obtained by high speed camera at $0.59 Q/Q_{Des}$ in the return channel.

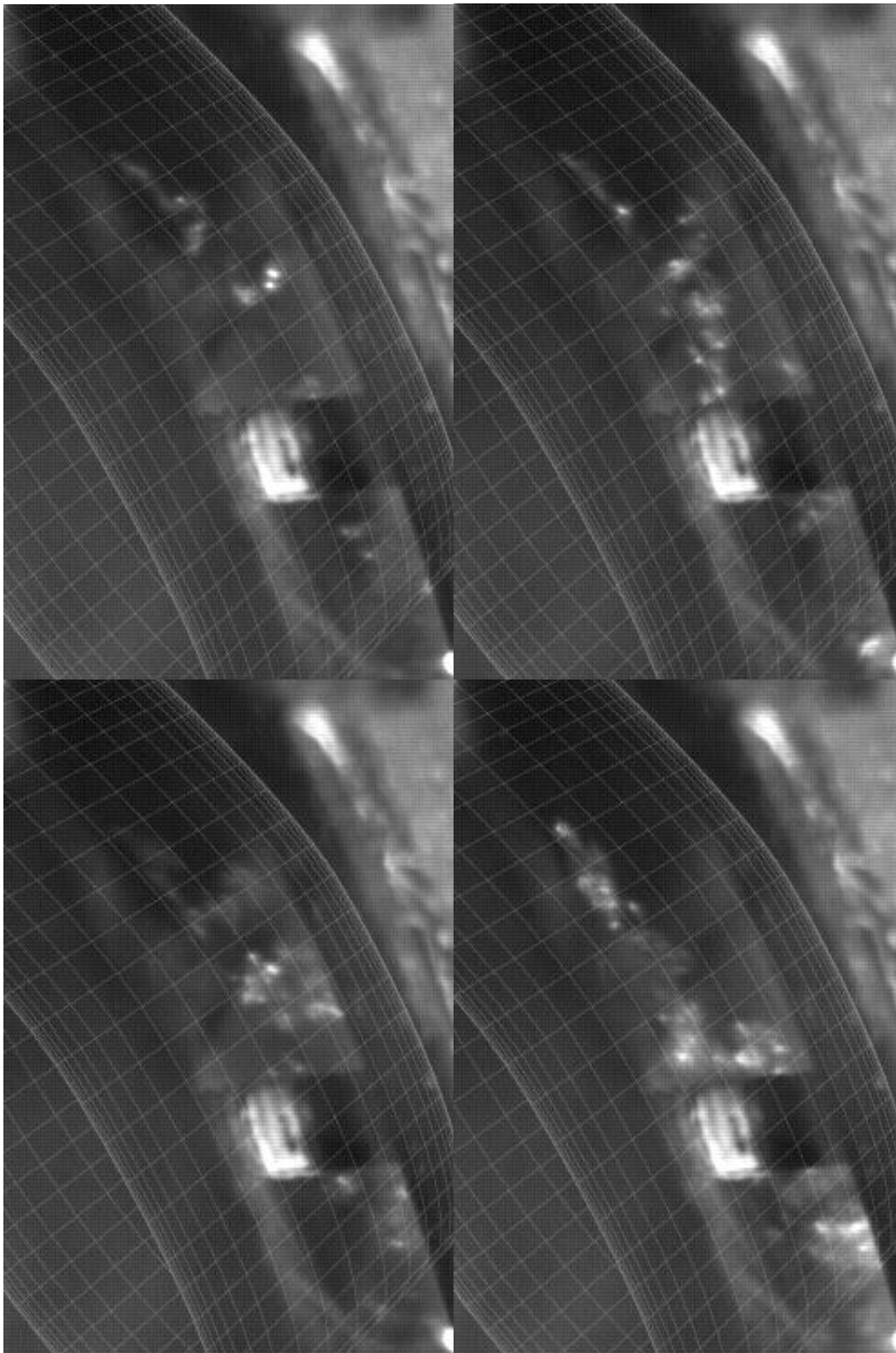
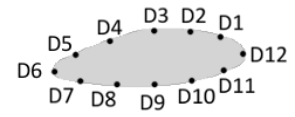
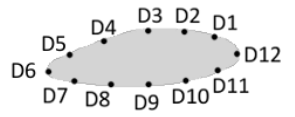


Fig. 16 Frames sequence obtained by high speed camera at $0.35 Q/Q_{Des}$ in the diffuser.

Table 1 Geometry characteristics and performance parameters of the tested pump-turbine.

Impeller data				
D_2 (mm)	B_2 (mm)	n_b	β_{2b} (°)	ϕ_{Des}
400	40	7	26.5	0.125
Diffuser vanes data				
D_3 (mm)	B_3 (mm)	n_b	α_{3b} (°)	λ (°)
410	40	22	10÷30	-8÷8
Return channel vanes data				
D_4 (mm)	B_4 (mm)	n_b	α_{4b} (°)	
516	40	11	30	

Table 2 Identified Independent frequency components.

Q/Q _{DES} [-]	St _S ≈ 0.335			St _F ≈ 0.6625		
	n° D3	n° D5	n° D6	n° D3	N° D5	n° D6
						
0.42	-	-	-	-	-	-
0.46	-	-	-	X	X	X
0.48	-	-	-	X	X	X
0.50	-	-	-	-	-	-
0.52	-	-	-	-	-	-
0.53	-	-	-	X	X	-
0.55	-	-	-	X	X	-
0.57	-	-	-	X	X	X
0.59	-	-	-	X	X	X
0.60	X	X	X	X	X	X
0.62	X	X	X	X	X	X
0.65	X	X	X	X	X	X
0.68	X	X	X	X	X	X
0.75	-	-	-	X	X	X
0.87	-	-	-	X	X	X
1.00	-	-	-	X	X	X
1.19	-	-	-	X	X	X